Fluctuating nonlinear spring theory

Maksudov, Farkhad; Kononova, Olga; Llauró, Aida; Ortega-Esteban, Alvaro; Douglas, Trevor; Condenzo, Gabriela N.; Martín, Carmen San; Marx, Kenneth A.; Wuite, Gijs J.L.; Roos, Wouter H.; de Pablo, Pedro J.; Barsegov, Valeri

published in
Acta Biomaterialia
2021

DOI (link to publisher)
10.1016/j.actbio.2020.12.043

document version
Publisher's PDF, also known as Version of record

Acta Biomaterialia 122 (2021) 263–277

Contents lists available at ScienceDirect

Acta Biomaterialia

journal homepage: www.elsevier.com/locate/actbio

Full length article

Fluctuating nonlinear spring theory: Strength, deformability, and toughness of biological nanoparticles from theoretical reconstruction of force-deformation spectra

Farkhad Maksudov[a], Olga Kononova[a,†], Aida Llauró[b], Alvaro Ortega-Esteban[b], Trevor Douglas[c], Gabriela N. Condezo[d], Carmen San Martín[d], Kenneth A. Marx[a], Gijs J.L. Wuite[e], Wouter H. Roos[f], Pedro J. de Pablo[b,*], Valeri Barsegov[a,*]

[a] Department of Chemistry, University of Massachusetts, Lowell, MA 01854, United States
[b] Department of Condensed Matter Physics and Condensed Matter Physics Center, Universidad Autónoma de Madrid, 28049, Madrid, Spain
[c] Department of Chemistry, Indiana University, Bloomington, IN 47405, United States
[d] Department of Macromolecular Structures and NanoBioMedicine Initiative, Centro Nacional de Biotecnología (CNB-CIC), Darwin 3, 28049 Madrid, Spain
[e] Department of Physics and Astronomy, and LaserLaB Amsterdam, Vrije Universiteit Amsterdam, De Boelelaan 1081, 1081 HV, Amsterdam, The Netherlands
[f] Moleculaire Biofysica, Zernike Instituut, Rijksuniversiteit Groningen, 9747 AG Groningen, The Netherlands

ARTICLE INFO

Article history:
Received 2 August 2020
Revised 16 December 2020
Accepted 17 December 2020
Available online 28 December 2020

Keywords:
Fluctuating nonlinear spring (FNS) model
Force-deformation spectra
Probability distribution of critical forces
Probability distribution of critical deformations
Fracture toughness

ABSTRACT

We developed the Fluctuating Nonlinear Spring (FNS) model to describe the dynamics of mechanical deformation of biological particles, such as virus capsids. The theory interprets the force-deformation spectra in terms of the "Hertzian stiffness" (non-linear regime of a particle's small-amplitude deformations), elastic constant (large-amplitude elastic deformations), and force range in which the particle's fracture occurs. The FNS theory enables one to quantify the particles' elasticity (Young's moduli for Hertzian and bending deformations), and the limits of their strength (critical forces, fracture toughness) and deformability (critical deformations) as well as the probability distributions of these properties, and to calculate the free energy changes for the particle's Hertzian, elastic, and plastic deformations, and eventual fracture. We applied the FNS theory to describe the protein capsids of bacteriophage P22, Human Adenovirus, and Herpes Simplex virus characterized by deformations before fracture that did not exceed 10–19% of their size. These nanoshells are soft (~1–10-GPa elastic modulus), with low ~50–480-kPa toughness – a regime of material behavior that is not well understood, and with the strength increasing while toughness decreases with their size. The particles' fracture is stochastic, with the average values of critical forces, critical deformations, and fracture toughness comparable with their standard deviations. The FNS theory predicts 0.7-MJ/mol free energy for P22 capsid maturation, and it could be extended to describe uniaxial deformation of cylindrical microtubules and ellipsoidal cellular organelles.

Statement of significance

Atomic Force Microscopy made it possible to probe material properties of biological particles, but these experiments yield results that are difficult to interpret. We developed the Fluctuating Nonlinear Spring (FNS) theory to describe force-deformation curves in the entire range of a biological particles' dynamic behaviors from the Hertzian indentation, to the bending deformation, and to the particles' fracture. We applied FNS theory to characterize bacteriophage P22, Human Adenovirus, and Herpes Simplex virus. These nanoshells are soft (1–10-GPa modulus) with low ~50–480-kPa toughness and weakly ductile. Larger particles are more resilient and plastic compared to smaller particles. The scope of potential applications

List of Notations used: x_H, (Hertzian) deformation of protein layer under the indenter; x_b, bending deformation of side portion (beams); x_b^*, maximum deformation of side portion before beams start to fail; X_H^*, maximum value of total deformation X in *Regime I* of Hertzian indentation; X_b^*, maximum value of total deformation X in *Regime II* of beam bending; F_b^*, maximum value of total force F in *Regime II* of beam bending; $\widetilde{x_H}(X)$, (Hertzian) deformation of protein layer as a function of total deformation X in *Regime III*; $x_b(\widetilde{X})$, bending deformation of side portion as a function of total deformation X in *Regime III*; K_b, elastic constant of the side portion of particle (curved beams); k_H, Hertzian spring constant of protein layer; $\widetilde{F}_b$, strength scale in Weibull distribution; X_{cr}, average critical (maximum) total deformation of the particle at fracture; F_{cr}, average critical (maximum) deformation force of the particle at fracture; m, shape parameter (mechanical cooperativity among the beams).

* Corresponding authors.
E-mail addresses: p.j.depablo@uam.es (P.J. de Pablo), valeri_barsegov@uml.edu (V. Barsegov).
† Department of Materials Science and Engineering, University of California, Berkeley, Berkeley, CA, USA.

https://doi.org/10.1016/j.actbio.2020.12.043

of the FNS theory is manifold; we estimated the free energy for P22 capsid maturation to be 0.7 MJ/mol.

1. Introduction

Virus nucleocapsids constitute an outstanding example of automatic nanomachines that perform complex functions, including self-assembly, selective packaging of nucleic acids, host recognition, and genome uncoating [1]. During their life cycle, viruses need to cope with a variety of mechanical constraints [2–4], and self-assembly of the virus particles requires both flexibility and weak interactions in order to correct for errors in the assembly process. After a fully infectious virion is produced, it is advantageous for a virus to possess a strong shell in order to survive in harsh environmental conditions. Yet, upon host infection, the shell again needs to display a certain degree of flexibility and softness, in order for the virus to deliver its genomic payload. In addition, virus particles require structures with exceptional properties to protect the cargo against various physico-chemical assaults during transport and to promote cargo release at the right moment and location [5]. Therefore, to understand the viral infectious pathway, it is necessary to scrutinize the mechanical properties of viruses. A single-particle approach to solve this problem is provided by Atomic Force Microscopy (AFM) based mechanical testing [6–10]. By using this mechanical approach a direct link between mechanics and infectivity of viral particles has been revealed [11].

To probe the physico-chemical and materials properties of virus shells, AFM is typically used in its force spectroscopy mode [10,12,13]. In these experiments, a cantilever tip (indenter) approaches a particle and gradually deforms the particle, while the restoring force (deformation force) F from the particle, corresponding to the particle deformation X is measured [7,8]. In a typical AFM nanoindentation assay, a compressive force is exerted on a particle through the indenter perpendicular to the particle surface, and so the stresses in the particle structure (around the indenter) are predominantly compressive. The force magnitude f is ramped up in time t with a force-loading rate r_f, i.e. $f = r_f\, t$ (force-ramp mode), until the irreversible particle fracture occurs. An array of different viruses and cell organelles have been experimentally characterized by profiling F as a function of X (FX-curve). These include: bacteriophages Φ29 [9,14,15] and HK97 [16], human viruses Noro Virus [17], Hepatitis B Virus [18], Human Immuno Deficiency Virus (HIV) [11], Adenovirus (HAdV) [19–22], and Herpes Simplex Virus [23,24], as well as other viruses infecting eukaryotic cells such as Minute Virus of Mice [25,26], Triatoma Virus (TrV) [27], rotavirus [28] and plant viruses, such as Cowpea Chlorotic Mottle Virus (CCMV) [29,30] and Brome Mosaic Virus (BMV) [31]. The experimental FX-curves reveal valuable information such as the particle stiffness, reversibility of deformation, and the forces required to break capsid structures.

A surprising diversity of mechanical properties of biological particles is revealed by AFM experiments. These properties have been shown to correlate with individual capsid structures' conformational dynamics [7,8] and they help to determine critical biological events in different parts of the viral infection cycle, such as capsid maturation, receptor binding, and genome uncoating [32]. The principal difficulty in gaining further energetic and structural insights into these important biological events is that experiments produce results that are difficult to interpret, which limits the scope of potential information gain. The problem is the lack of any comprehensive theoretical model that describes the full range of a capsid's observed mechanical behaviors from the small-scale indentation to the large-scale deformation, and to the particle's fracture. There are several aspects of the nanomechanics of virus particles that are not well understood. Why is the initial portion of the FX spectra non-linear? What particle features determine their mechanical limits, i.e. the critical forces, critical deformations, and particle's toughness? Why do the FX spectra for the same particle differ from one measurement to another? The latter property points to thestochastic nature of their deformation and fracture. Yet, the question remains: what defines the occurrence of a particle's fracture at a given force load? Virus particles are typically characterized by their stiffness; yet, *in silico* nanoindentation studies reveal that the derivative of the particle indentation force with respect to indentation (dF/dX), which quantifies particle stiffness, fluctuates significantly with X [33]. A related question is: what are the mechanisms of structure remodeling that give rise to the non-monotonic behavior for F vs. X? Currently, there is a lack of understanding of the underlying physical picture that describes the dynamic mechanical behavior of capsids and other types of nanoshells subject to external mechanical factors. There is a pressing need for a unified theoretical framework to interpret and model the experimental FX-spectral lineshapes available from the AFM-based mechanical testing experiments.

Despite a great increase in our knowledge of the biomechanics of virus capsids, much about the mechanisms underlying a capsid's mechanobiology remains unexplored. In particular, little is known about what causes the biological particles to fracture and fail mechanically, even though there is a wealth of knowledge about the biomechanical properties of their intact capsids. The microscopic mechanism(s) of a particle's fracture determines its fracture toughness – a defining material property of all biological matter, which quantifies the resistance of a particle to fracture and subsequent loss of mechanical properties (mechanical failure). Although the fracture behavior of materials has long been critically important for understanding many non-biological systems, including hydrogels [34,35] among more recent examples studied, its application to the fracture of viral capsids is a hot research topic. Moreover, virus capsids are heterogeneous structures formed by non-covalently coupled capsomer repeats, but the fracture criteria in heterogeneous biomaterials are poorly understood. It is not clear how to draw a borderline separating the plastic deformation from the particle's fracture.

We employed mechanical nanomanipulations *in silico* in previous studies to explore the dynamics of uniaxial mechanical deformation and fracture of thick soft spherically shaped biological particles. These included studies of the Cowpea Chlorotic Mottle Virus (CCMV) capsid, the bacterial nanocompartment encapsulin, and thick soft cylindrical microtubule filaments, structural elements found in all eukaryotic cells [36–39]. We used the output from these simulations to perform extensive analysis of the structural alterations in these particles and propagation and redistribution of potential energy and Cauchy stress in different portions of their structure. By correlating the simulated FX-spectra collected using the experimentally relevant dynamic force-loading conditions with the structure and shape alterations and with the changes in energy and stress in these biological particle models, we were able to identify the types of mechanical deformations (or mechanical excitations) that define the dynamics of their compressive force induced deformation and fracture. The emerging microscopic physical picture laid the foundation for proposing the Fluctuating Nonlinear Spring (FNS) model of mechanical deformation

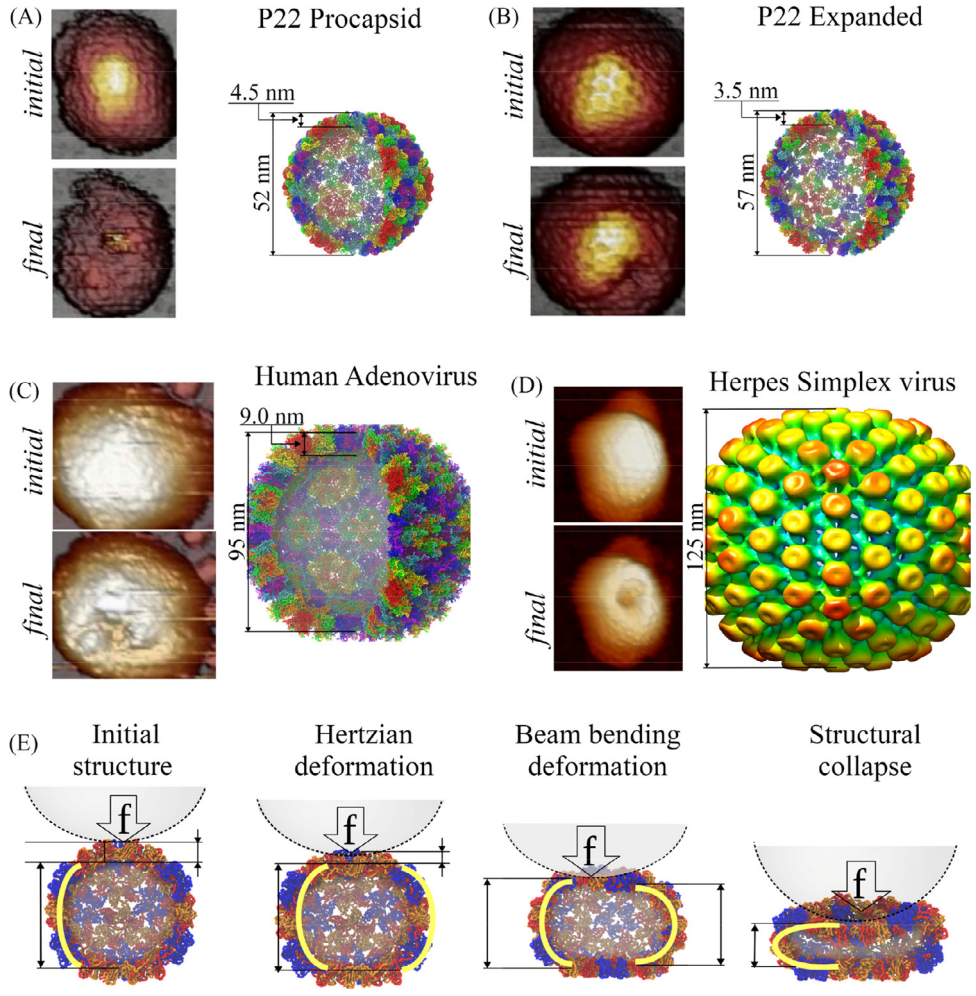

Fig. 1. High-resolution AFM images and structure snapshots of the virus capsids. Displayed are bacteriophage P22 Procapsid shell (**A**) and bacteriophage P22 Expanded shell (**B**), Human Adenovirus capsid (**C**), and Herpes Simplex virus capsid (**D**). On the left in each panel are the most representative experimental images obtained before (top) and after (bottom) indentation. On the right in each panel are the X-ray structures of the capsids with their size and thickness obtained from the Protein Data Bank (PDB). The PDB codes: 3IYH (P22 Procapsid), 3IYI (P22 Expanded shell [66]), and 3IYN (Human Adenovirus [67]). The structure of the Herpes Simplex virus was reconstructed from the Cryo-electron map (Electron Microscopy Data Bank entry: EMD-1959 [68]); the estimated thickness of Herpes Simplex virus capsid is ~4 nm. Panel **E** illustrates for a soft CCMV capsid the mechanical degrees of freedom corresponding to the *Hertzian indentation regime I, beam-bending regime II* and *particle fracture regime III*. Also shown are changes in the three-dimensional structure of the CCMV shell from the intact capsid (initial structure on the left) through the weakly and strongly deformed capsid (snapshots in the middle) to the collapsed particle (snapshot on the right).

of thick soft nanoshells [33]. The only drawback was that the theoretical force-deformation spectra were constructed using numerical calculations, which reduces the interpretability and offers little mechanistic understanding of the results obtained.

Here, we took a step further to develop an analytically tractable theoretical framework to describe the nanomechanics of spherically-shaped soft biological particles such as virus capsids, and to interpret their *FX*-spectra accessible in single-particle mechanical testing experiments *in vitro* and *in silico*. This theory is based on the FNS model [33], which links directly the dynamic structural alterations in biological particles to the stochastic nature of dynamics of their deformations and describes structural damage to account for the particle's fracture. To map the physical picture underlying deformation and fracture of biological particles into a mathematical framework, the FNS theory considers the small-amplitude Hertzian indentation of the particle's protein layer under the indenter (cantilever tip used in AFM), large-amplitude bending deformation of the particle side portion for force loads below the critical threshold, and fracture and structural collapse of the particle for force loads exceeding the limits of the particle's mechanical strength. In this study, the theory is applied to provide meaningful interpretation and modeling of the *FX*-spectra for soft protein shells of bacteriophages P22 in the Procapsid state and Expanded state, and capsids of Human Adenovirus and Herpes Simplex virus displayed in Fig. 1. This choice of protein capsids provides us with a broad range of particle sizes (~52–125 nm) and values of the thickness (~3.5–9 nm).

Excellent agreement was observed between the experimental and theoretical *FX*-spectra, demonstrating that the FNS model captures the dynamics of the different capsid particles' deformation and collapse. The theory describes the fine features of the *FX*-spectra as observed in single-particle mechanical testing experiments [40]. The FNS theory uses the *FX*-spectra as an input to determine not only the ensemble average mechanical properties of biological particles, such as the average critical force and critical deformation, and the material properties such as the Young's moduli for Hertzian indentation and bending deformations, which carry valuable information about the physical range and limits of particles' mechanical strength and deformability, but it also to maps out the entire distributions of these properties, i.e. the probability distributions of critical forces and critical deformations. Furthermore, the FNS theory can be applied to calculate the thermody-

namic state functions, including the free energy changes associated with the particle's Hertzian indentation, elastic deformation, plastic deformations, and the particle's fracture. Moreover, using the FNS theory makes it possible to determine the ensemble average and distribution of fracture toughness of biological particles the property of a material to absorb energy and deform without breaking.

2. Materials and methods

2.1. Experimental methods

Single-particle AFM experiments: The AFM nanoindentation experiments were conducted as described elsewhere [41]. Briefly, a virus capsid was imaged and zoomed-in continuously by reducing the *xy*-scanning size until the individual particle was framed in the scanning area. Then, the lateral piezo scan was stopped when the tip was on top of the particle. The virus shell was deformed with the AFM tip by performing individual indentation. In AFM experiments, we employed the dynamic force-ramp, in which the applied compressive force $f(t)$ increases linearly with time t with the force loading rate r_f until irreversible particle fracture occurs. For this reason, the maximum force applied during each indentation measurement was sufficient to induce the capsid deformation and fracture. The force-deformation curves (*FX* curves), which quantify deformation of the particle, were obtained from the curves of force versus *Z* piezo (*FZ* curves), which includes deformations of the cantilever tip and the particle, by subtracting the compliance of the cantilever.

Bacteriophage P22: AFM experiments were performed as described previously in Llauró et al. [42,43]. Experiments were done with a Nanotec Electrónica microscope (Madrid, Spain) operating in Jumping Mode Plus [44]. The AFM experiments on empty Bacteriophage P22 particles were performed at a controlled temperature of 17 °C. Imaging forces were kept between 60 and 150 pN. Rectangular silicon-nitride cantilevers (RC800PSA, Olympus, Center Valley, PA) with an approximate tip-radius R_{tip}= 20 nm and the spring constant κ = 0.05 N/m were used. Before each measurement, cantilevers were calibrated using Sader's method [45]. For P22 samples, experiments were carried out in buffer conditions (100 mM phosphate, 50 mM NaCl, pH 7). A 20 µL drop of 100-fold diluted stock solution was incubated on a silanized glass coverslip. After 30 min, the sample was washed with buffer solution until a volume of 90 µL was reached. AFM images were processed with the WSxM software [46]. The slow probe velocity v_f = 100–150 nm/s was used.

Human Adenovirus: As previously described [22], empty Human Adenovirus (HAdV) capsids corresponds to the light-density particles produced by the HAdV-C5 delayed packaging mutant FC31 (FC31-L3) [47], which was propagated at 37 °C in HEK293 cells and harvested at 56 h post-infection. Particles were purified by equilibrium centrifugation in two consecutive CsCl gradients, desalted on a Bio-Rad 10 DC column, and stored in HBS buffer (20 mM Hepes, 150 mM NaCl, pH 7.8) supplemented with 10% glycerol for long-term storage at −80 °C. Short-term stored single-use aliquots (5 μL) [21] of empty HAdV particles FC31-L3 [47] were diluted in HBS to obtain a final concentration of 5 mM Ni^{2+} and adsorbed onto freshly cleaved Muscovite mica (V-1 quality). The sample was incubated for 20 min at 4 °C before washing with 5 mM $NiCl_2$ in HBS. The mica was placed on the AFM sample holder and immersed in the buffer solution up to a total volume of 530 μL. The AFM tip was pre-wetted with 30 μL of the same buffer [22]. Single empty HAdV particles were located on the mica surface [22] by operating the AFM in Jumping Mode Plus [44] at low forces in liquid, using rectangular RC800PSA cantilevers (Olympus, Tokyo, Japan) with an approximate tip-radius R_{tip} = 20 nm and the spring constants of 0.05 N/m. Cantilever spring constants were calibrated with the Sader method [45]. Images and curves were processed using the WSxM software [46]. The probe velocity v_f was about 100–150 nm/s.

Herpes Simplex virus: Nuclear A-type capsids were isolated from cells infected with WT HSV-1 strain F, ATCC VR-733 by sucrose gradient sedimentation as described previously [24,48,49]. The Herpes Simplex virus (HSV) particles were deposited on silanized glass substrates and analyzed in buffer conditions (50 mM Tris, 150 mM NaCl, pH 7.5) by AFM imaging and nanoindentation as described in detail elsewhere [24,30,41]. Experiments were performed using a Nanotec Electrónica microscope (Madrid, Spain). Cantilevers with an approximate tip-radius of R_{tip},= 15 nm and a spring constant of κ = 0.05 N/m (Olympus OMCL-RC800PSA) were used at a slow probe velocity v_f = 60 nm/s.

2.2. Fluctuating nonlinear spring model

Mechanical excitations: Prior Langevin Dynamics simulations of uniaxial deformation of CCMV capsid [36], bacterial nanocompartment encapsulin [37], and microtubule filaments [38] revealed that these protein structures can be described using the following mechanical degrees of freedom: i) small-amplitude inelastic Hertzian indentation of a protein layer under the indenter (cantilever tip); and ii) large-amplitude elastic bending deformation of the capsid side portion, which constitutes the major part (>90%) of the structure (Fig. 1E; see also Fig. S1 in the Supporting Information (SI)). These types of mechanical deformations are graphically illustrated for the CCMV shell in Fig 1E (see also Fig. S1). Based on this decomposition into the Hertzian indentation and beam-bending deformation, the FNS model partitions the capsid particle into the top portion and the side portion. The top portion can be viewed as a "Hertzian cushion", which makes the particle-indenter physical contact. The initial Hertzian indentation dominates the weakly inelastic *regime I* (Figs. 1E and S1). The capsid side portion can be represented most simply as a side barrel, which is formed by a collection of curved beams arranged along the capsid circumference. The beamscooperate to withstand the stress due to mechanical loading (Fig. 1E). The beam-bending elastic response defines the linear *regime II* (Figs. 1E and S1). Yet, the beams can break when the stress exceeds some threshold, and the particle fractures when the longest lasting (strongest) beam fails. In *regime III*, both the Hertzian indentation and beam-bending deformation contribute to the total mechanical response (total force) of the particle (Figs. 1E and S1). We can describe the likelihood of beams' failure most simply by using the damage probability, which increases with the particle's deformation (X). In the remainder of this section, we describe in more detail the mechanical degrees of freedom (Hertzian indentation and beam-bending deformation), the likelihood of structural damage (probability of beams breakage), and the contribution of these elements of the FNS model to the total mechanical response. [Notations used in this paper (listed in the SI) are improved, and hence, slightly different from those used in Ref. [33]].

The *Hertzian indentation* x_H, occurs due to direct mechanical interaction between the protein layer of a finite thickness and the cantilever tip, which progressively indents the particle's surface (Fig. 1E). The Hertzian force response F_H is given by [50]

$$F_H(x_H) = k_H x_H^{3/2} \tag{1}$$

In Eq. (1) above, $k_H = (R_{par}R_{tip}/(R_{par}+R_{tip}))^{1/2}/D_H$ is the Hertzian stiffness (constant prefactor), and R_{par} and R_{tip} are the particle and tip radii, respectively; also, $D_H = 0.75((1-\sigma_H^2)/E_H + (1-\sigma_{tip}^2)/E_{tip})$, where E_H and E_{tip} are the Young's moduli and σ_H and σ_{tip} are the Poisson's ratios for the par-

ticle and the tip, respectively. Since $E_H << E_{tip}$, $D_H = 0.75(\frac{1-\sigma_H^2}{E_H})$ [33,50]. The bending force F_b due to *deformation of a curved beam* x_b is described by Hooke's law (see Ref. [33,50] for more detail),

$$F(x_b) = k_b x_b \tag{2}$$

where $k_b = 9E_bI\pi/8R_{par}^3$ is the elastic constant of each beam (spring constant for bending of curved beams), and E_bI is the beam's flexural rigidity given by the product of the Young's modulus for bending E_b and the moment of inertia I [33]. The experimentally measurable total deformation X is given by the sum of Hertzian and beam-bending deformations, i.e.

$$X = x_H + x_b \tag{3}$$

Damage probability: In the FNS model, the side portion of a virus particle's structure is described by a collection of curved beams arranged in parallel along the capsid circumference [33]. Each beam responds to bending deformation x_b with the (average) stiffness k_b, resulting in the total stiffness of capsid side portions $K_b = Nk_b$, where N is number of beams. The structural collapse at a critical force can be represented by the mechanical failure of these structural elements. At any given moment, there are n beams that have failed and $(N-n)$ beams that have survived, and so the actual beam bending force is

$$F_b(x_b) = k_b(N-n)x_b = K_b x_b(1-n/N) \tag{4}$$

In Eq. (4), $s = 1 - n/N$ is the particle survival probability. In the continuous limit of large N, the discrete probability s can be replaced by the continuous probability. Because the longest-lasting beam determines the onset of a particle's fracture when the force and deformation exceed the critical level [33], we use the Weibull distribution to describe the survival probability [51]

$$s(x_b) = \exp\left[-\left(F_b/\widetilde{F}_b\right)^m\right] = \exp\left[-\left(K_b x_b/\widetilde{F}_b\right)^m\right] \tag{5}$$

In Eq. (5), the strength scale parameter $\widetilde{F}_b$ represents a range of forces, in which the beams fail. The shape parameter m quantifies the mechanical cooperativity due to dynamic coupling among the curved beams. When $m = 1$ the beams are independent, they break one-by-one, which corresponds to the simple exponential distribution for the survival probability $\exp[-(K_b x_b/\widetilde{F}_b)]$. When $m > 1$, the structural elements (beams) are coupled and they cooperate to withstand the stress.

Deformation force: The equation for the total deformation force $F(x_H, x_b)$ is given by

$$F(x_H, x_b) = F_H(x_H) + F_b(x_b) = k_H x_H^{3/2} + K_b x_b s(x_b) \tag{6}$$

The total mechanical response (deformation force) is a bivariate function $F(x_H, x_b)$ expressed in terms of the Hertzian indentation x_H and beam-bending deformation x_b (see Fig. S1), whereas in AFM experiments F is a function of the total deformation, $X = x_H + x_b$, i.e. $F = F(X) = F(x_H + x_b)$. In general, $F(x_H, x_b)$ given by Eq. (6) can be converted into $F(X = x_H + x_b)$ using the method of Lagrange multipliers. In our previous study [33,37], we found that $m = 1$–2 for different capsids, which means that the curved beams forming the side portion of particle's structure are weakly coupled, and so here we used a weak coupling approximation ($m \approx 1$). Then, Eq. (5) transforms into the exponential distribution $\exp[-F_b/\widetilde{F}_b] = \exp[-K_b x_b/\widetilde{F}_b]$, and the calculations of $F(X = x_H + x_b)$ and other physical quantities are much simplified. Because the main goal in this current study is to derive the analytical expressions for the force-deformation lineshape in all three *regimes I-III* (see Eqs. 7), we set $m = 1$. This allows us to obtain a closed-form analytical expression for the deformation force $F(X)$ (see Results).

3. Results

Dynamic regimes for uniaxial mechanical deformation of biological particles: Our *in silico* nanoindentation experiments on soft particles – Cowpea Chlorotic Mottle Virus (CCMV) capsid [33,36,39], bacterial nanocompartment encapsulin [37], and microtubule (MT) filament fragments [38], showed that the mechanical response of thick soft biological particles subject to uniaxial deformation can be divided into the following three regimes (displayed in Figure S1A-C): weakly non-linear *Hertzian indentation regime I*, linear elastic *beam deformation regime II*, and *particle fracture regime III*. These mechanical regimes are illustrated in Figs. 1E and S1 using a typical force (F)–deformation (X) spectrum (*FX*-curve) and structure snapshots for the CCMV capsid [33]. The in-depth analysis of the structures and distributions of stresses in soft CCMV and MT particles showed that, initially, the mechanical stress accumulates in the protein layer underneath the indenter (cantilever tip), and only in later stages of compression does the stress propagate to the side portions of the structure [36,38]. The accumulation and subsequent redistribution of stress triggers different mechanical excitations associated with the Hertzian indentation of the protein layer around the cantilever tip and bending deformation of the curved-beam-like side portion of the particle's structure. At different stages of deformation, these Hertzian and beam-bending deformation degrees of freedom contribute differently (see Fig. S1). The capsids of bacteriophages P22 in the Procapsid state and Expanded state, Human Adenovirus (HAdV), and Herpes Simplex Virus (HSV) also form soft and thick particles (Fig. 1). In the case of the bacteriophage P22 particle, the maturation process involves the expansion of the prohead which results in the volume increase of ~35% as well as in the capsid thinning and decrease in porosity. Not surprisingly, the *FX*-curves for these particles (Fig. 2) and for the CCMV capsid (Fig. S1A) look very similar. Below, we consider these three dynamic regimes of mechanical deformation and collapse separately (see Fig. S1A).

Hertzian indentation regime I: Initially, mechanical stress is localized in the protein layer underneath the cantilever tip, which results in local curvature change and deformation of the protein layer (see structure snapshots in Fig. 1E). In this regime, the profile of typical *FX*-curves is slightly non-linear, i.e. $F \sim X^{3/2}$ (Fig. S1A; see also Fig. S1B) for $0 \le X \le X_H^*$, where X_H^* is the maximum value of Hertzian indentation x_H. In this regime, we can neglect the beam-bending deformation ($x_b = 0$) and consider only the contribution from x_H, i.e. $x_H = X$ (Fig. S1B). Using Eqs. (1) and (6), we obtain for this regime: $F(X) = F(x_H) = k_H X^{3/2}$, for $0 \le X \le X_H^*$.

Beam-bending deformation regime II: After the Hertzian degree of freedom x_H has been fully excited ($x_H = X_H^*$), the compressive force triggers excitation of the bending degrees of freedom associated with the deformations of curved beams, $x_b = X - X_H^*$ (see Fig. S1B). The force response is elastic $F \sim X$ (Fig. S1A; see also Fig. S1B), and the beams remain intact (see structure snapshot in Fig. S1F). This is reflected in constant survival probability: $s(x_b) = 1$ while the regime lasts (Fig. S1C). This regime continues in the range $X_H^* \le X \le X_H^* + x_b^* = X_b^*$, where x_b^* and X_b^* are, respectively, the maximum deformation of each beam and total particle deformation right before the beams start to fail. Using Eqs. (2) and (6), we obtain (see SI for derivation): $F(X) = F(x_H, x_b) = k_H(X_H^*)^{3/2} + K_b(X - X_H^*)$, for $X_H^* \le X \le X_b^*$.

Particle fracture regime III: Beyond the elastic limit attained at $X = X_b^*$ and as soon as mechanical load starts exceeding the structural stability threshold, the beams start yielding to a compressive force, which corresponds to a decrease in the survival probability $s(x_b)$ (see Fig. S1C), and the particle transitions to the collapsed state (structure snapshot in Fig. S1G). The force response deviates from the linear scaling, i.e $F \sim -X^{3/2}$ (Fig. S1A). In this regime, both x_H and x_b contribute to the total deformation X for

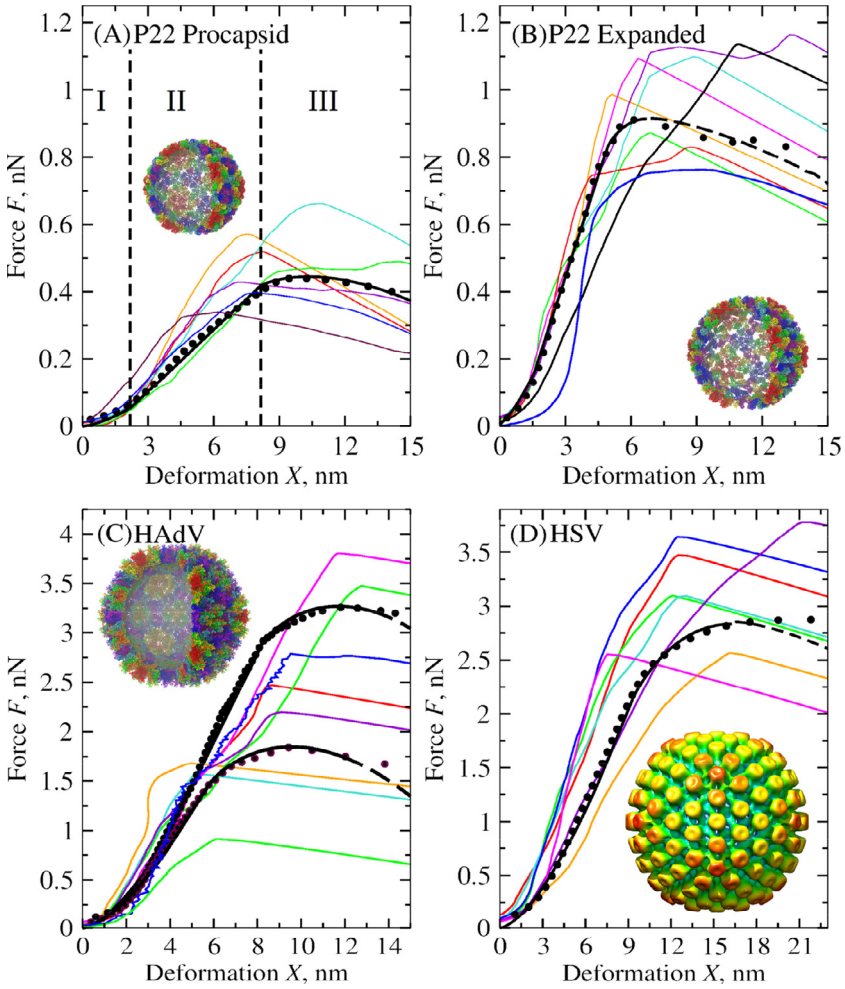

Fig. 2. AFM-based compressive deformation of biological particles. Displayed in different colors are the experimental force(*F*)-deformation(*X*) spectra (solid lines) and theoretical *FX*-curves for bacteriophage P22 Procapsid shell (**A**) and Expanded bacteriophage P22 shell (**B**), Human Adenovirus capsid (**C**), and Herpes Simplex virus capsid (**D**). The average experimental *FX*-spectra (black data points) are compared with the theoretical *FX*-curves obtained using the FNS theory (black solid and dashed lines). The dashed lines are continuations of the solid lines, which denote the actual fit of Eqs. (7) to the experimental force-deformation data points, past the collapse transition when the particle fractures. Also shown in panel **A** are the *Hertzian indentation regime I, beam-bending regime II* and *particle fracture regime III* for P22 Procapsid. For Human Adenovirus showing the strong and weak mechanical response (black data points and lines), we display two average *FX*-spectra overlaid with the theoretical *FX*-curves. (For interpretation of the references to color in this figure legend, the reader is referred to the web version of this article.)

$X > X_b^*$ (see Fig. S1B). Using Eqs. (6) above, we obtain for this regime the following expression (see SI): $F(X) = -k_H(X - X_b^*)^{3/2} + \frac{9k_H^2\tilde{F}_b}{16K_b^2}(X - X_b^*) + \tilde{F}_b - \frac{9k_H^2\tilde{F}_b^2}{16K_b^3} + \frac{27k_H^4\tilde{F}_b^3}{512K_b^6}$, for $X > X_b^*$. Regime III is a mixture of elastic and plastic deformation behaviors. The post-collapsed regime (Fig. S1A-C) corresponds to the failure of the beams (structure snapshots in Fig. S1C), which results in the particle's fracture and subsequent release of elastic energy stored in the particle.

Application of FNS theory: Under slow force-loading conditions, which correspond to using slow probe velocities v_f = 60–150 nm/s, when the particle structure equilibrates on a timescale faster than the rate of force increase ($r_f = kv_f$), a stochastic path $F = F(x_H, x_b)$ (Eq. (6)) follows closely the equilibrium deformation path (quasi-equilibrium). The equilibrium force response from the biological particle can then be determined using the condition that the deformation energy (ΔG) attains the minimum at each value of total deformation X. The minimum of the energy $\Delta G(X) = \int_0^X F(X')dX'$ (i.e. the integral or the area under the *FX*-curve) at each value of X corresponds to the minimum of the force (i.e. the integrand $F(X')$) at each X, and so the condition of minimum deformation energy translates to finding the minimum deformation force F (see Ref. [33] for more detail). This can be accomplished using the method of Lagrange multipliers, i.e. finding the minimum of $F(x_H, x_b)$ subject to the constraint, $X = x_H + x_b$ (see SI for detail).

In the weak cooperativity limit ($m \approx 1$), the master equation for $F(X)$ in *regimes I-III* reads:

$$F(X) = \begin{cases} B_0 X^{3/2}, \quad 0 \le X \le X_H^* = \frac{9k_H^2\tilde{F}_b^2}{64K_b^4} & (\textit{regime I}) \\ B_0\left(X_H^*\right)^{3/2} + B_1\left(X - X_H^*\right), \quad X_H^* < X < X_b^* = \frac{\tilde{F}_b}{K_b} - \frac{27k_H^2\tilde{F}_2^b}{64K_b^4} & (\textit{regime II}) \\ -B_0\left(X - X_b^*\right)^{3/2} + B_2\left(X - X_b^*\right) + B_3, \quad X_b^* \le X \le X_{cr} = \frac{\tilde{F}_b}{K_b} - \frac{9k_H^2\tilde{F}_b^2}{32K_b^4} & (\textit{regime III}) \end{cases} \tag{7}$$

Table 1
Parameters of FNS model for uniaxial deformation of P22 virus shells, human Adenovirus (HAdV) capsid, and Herpes Simplex virus (HSV) capsid (see Fig. 2): Hertzian spring constant k_H, stiffness constant K_b, and force range $\widetilde{F}_b$. The parameter values are obtained from the fit of theoretical *FX*-curves (Eqs. (7)) to the experimental *FX*-spectra Fig. 2), and theoretical profiles of $p(F)$ to the histograms of critical forces (Eq. (13)) (Fig. 3; separated by the slash). For HAdV, two sets of values for the weak and strong mechanical responses, are reported. We also compared the theoretical values of the average critical force F_{cr} and average critical deformation X_{cr}, obtained using Eqs. (8) and ((9), respectively, and the experimental values of these quantities extracted from the experimental *FX*-spectra (separated by the slash). Also, compared are the Young's moduli for Hertzian deformation E_H and bending deformation E_b obtained with Eqs. (10) and (11), respectively. The values of E_b obtained using Eq. (11) and the thin shell approximation (see Discussion) are separated by a slash.

Particle	FNS model parameters			Critical forces and critical deformations		Young's moduli	
	k_H, nN/nm$^{3/2}$	K_b, nN/nm	$\widetilde{F}_b$, nN	F_{cr}, nN	X_{cr}, nm	E_H, GPa	E_b, GPa
P22 Procapsid	0.02/0.02	0.06/0.04	0.90/0.39	0.46/0.45	9.8/10.3	0.03	0.25/(0.2–0.4)
P22 Expanded	0.06/0.06	0.18/0.18	2.07/0.64	0.90/0.92	6.2/7.5	0.12	1.86/(1.1–2.1)
HAdV weak	0.10/0.11	0.32/0.38	5.10/1.01	1.86/1.96	9.5/9.2	0.22	0.43/(0.42–0.82)
HAdV strong	0.12/0.12	0.46/0.50	9.91/2.12	3.50/3.80	12.8/13.4	0.27	0.62/(0.6–1.2)
HSV	0.07/0.07	0.30/0.30	7.01/2.31	2.60/2.72	14.0/14.4	0.17	10/(3.0–5.9)

where $B_0 = k_H$, $B_1 = K_b$, $B_2 = \frac{9k_H^2\widetilde{F}_b}{16K_b^2}$ and $B_3 = \widetilde{F}_b - \frac{9k_H^2\widetilde{F}_b^2}{16K_b^3} + \frac{27k_H^4\widetilde{F}_b^3}{512K_b^6}$ are constant coefficients. Eqs. (7) can be used to describe the dynamics of uniaxial mechanical deformation of virus particles in the entire deformation range. In regime III, the critical force for particle fracture, i.e. the force maximum F_{cr} in the *FX*-curve, is given by

$$F_{cr} = \widetilde{F}_b - \frac{9k_H^2\widetilde{F}_b^2}{16K_b^3} + \frac{81k_H^4\widetilde{F}_b^3}{1024K_b^6} \tag{8}$$

and the critical deformation X_{cr} is given by (see SI for derivation):

$$X_{cr} = \frac{\widetilde{F}_b}{K_b} - \frac{9k_H^2\widetilde{F}_b^2}{32K_b^4} \tag{9}$$

When F reaches F_{cr}, the beams fail and the particle fractures, which results in the force decreasing below F_{cr} for $X > X_{cr}$. We applied the master Eq. (7) to model the *FX*-curves and Eqs. (8) and (9) to predict the values of F_{cr} and X_{cr}, which quantifies the average strength and average deformability of a thick spherical shell, respectively.

Theoretical modeling of force-deformation spectra: The results of AFM experiments for all four model particles, including the *FX* curves and particles' images, were critically analyzed. Based on the experimental images before and after indentation, 7–10 representative *FX*-spectral curves have been extracted for each virus shell that were then running-averaged and aligned relative to the origin of the coordinate system (i.e. $X = 0$, $F = 0$ point). The most representative *FX*-curves are displayed in Fig. 2 (see Fig. S2 for all experimental *FX*-curves). For each particle, we calculated the average *FX*-curve (Fig. 2). Next, we applied the FNS theory to interpret the *FX*-curves and to characterize the dynamic mechanical properties of virus capsids in the *deformation regimes I-III*.

The FNS model has the following three parameters: 1) k_H – the mechanical characteristics of the particle's top protein layer under the indenter. This parameter reflects the inelastic component of the particle's deformation in the weakly nonlinear *regime I* of Hertzian deformation, and it can be determined by using the nonlinear curve fitting (first Eq. (7)) to the experimental *FX*-curve in *regime I*; 2) K_b – the mechanical characteristics of the particle's side portion. This parameter quantifies stiffness of the side portion of the particle's structure (curved beams) in *regime II* of their elastic deformation, and it can be determined by fitting a straight line (second Eq. (7)) to the experimental *FX*-curve in *regime II*; 3) $\widetilde{F}_b$ – the force scale parameter which enters the Weibull distribution (Eq. (5)). This parameter provides information about the physical range of deformation forces, in which the particle's fracture occurs; $\widetilde{F}_b$ can be determined from the fit of a nonlinear curve (third Eq. (7)) to the *FX*-profile in *regime III*.

We performed a numerical fit of the average *FX*-curves in all *regimes I-III* using, respectively, the first, second, and third Eq. (7). The results displayed in Fig. 2 show that the FNS theory accurately describes fine features of the *FX* spectral lineshapes for all virus capsids. The corresponding values of the Hertzian constant k_H, stiffness K_b, and strength parameter $\widetilde{F}_b$ are accumulated in Table 1. Analysis of the *FX*-spectra for the HAdV capsid showed that, unlike the other particles, this capsid displays both strong and weak mechanical responses characterized, respectively, by the larger experimental values of the critical force F_{cr}^{exp}= 3.8 nN and critical deformation X_{cr}^{exp}= 13.4 nm and smaller experimental values of F_{cr}^{exp}= 1.9 nN and X_{cr}^{exp}= 9.2 nm. This might be due, e.g., to different orientations of HAdV capsid on the substrate surface, which resulted in the particle indentations along different symmetry axes (Fig. 2C; see also Fig. 3C). We only found the bimodal mechanical response for the HAdV capsid due to different orientations of HAdV capsid on the substrate surface. The other particles displayed the unimodal mechanical response. These results agree with previous findings of the influence of the adsorption orientation-dependent symmetry axes in contact with the indenter tip on the mechanical properties of virus particles [19,25]. For this reason, we modeled the weak and strong mechanical response data for the HAdV capsid separately (Figs. 2–4 and Table 1).

We found that the Hertzian stiffness k_H correlates with the thickness h (see Table 1 and Fig. 1), which increases from ~3.5–4.5 nm for P22 capsid to ~9 nm for HAdV, and so does k_H which increases from ~0.02–0.06 nN/nm$^{3/2}$ to ~0.1–0.12 nN/nm$^{3/2}$. While the maximum thickness of the Herpes Simplex Virus (HSV) capsid is roughly 15 nm, the contiguous thickness (shell thickness) of HSV is only ~4 nm [24]. This explains a decrease in k_H to 0.07 nN/nm$^{3/2}$ for the HSV capsid. We found that the elastic constant K_b correlates with the particle size (Table 1 and Fig. 1). Indeed, K_b increases from ~0.06–0.18 nN/nm for the P22 capsid with size ~52–57 nm to ~0.32–0.46 nN/nm for HAdV with size ~95 nm. We also analyzed the strength scale $\widetilde{F}_b$ (see Eq. (5)). This quantity corresponds to the range of forces, in which the particle fracture and structural collapse occurs (i.e. peak forces in the *FX*-curves; see Fig. 2) due to stochastic variability. We found that $\widetilde{F}_b$ scales with particle size (see Table 1). For example, $\widetilde{F}_b$ increases from ~1–2 nN for the P22 virus capsid of size ~52–57 nm to ~5–10 nN for HAdV and HSV capsids with size ~95–125 nm (Fig. 1).

Next, we estimated the average values of critical force F_{cr} and critical deformation X_{cr} using Eqs. (8) and (9) for X_{cr} and parameters k_H, K_b and $\widetilde{F}_b$ from Table 1. Theoretical estimates of F_{cr} and X_{cr} are compared in Table 1 with their experimental values extracted from the average *FX*-curves (Fig. 2). Overall, the theoretical predictions for F_{cr} and X_{cr} agree very well with the experimental values (Table 1). We found that F_{cr} and X_{cr} are not directly correlated,

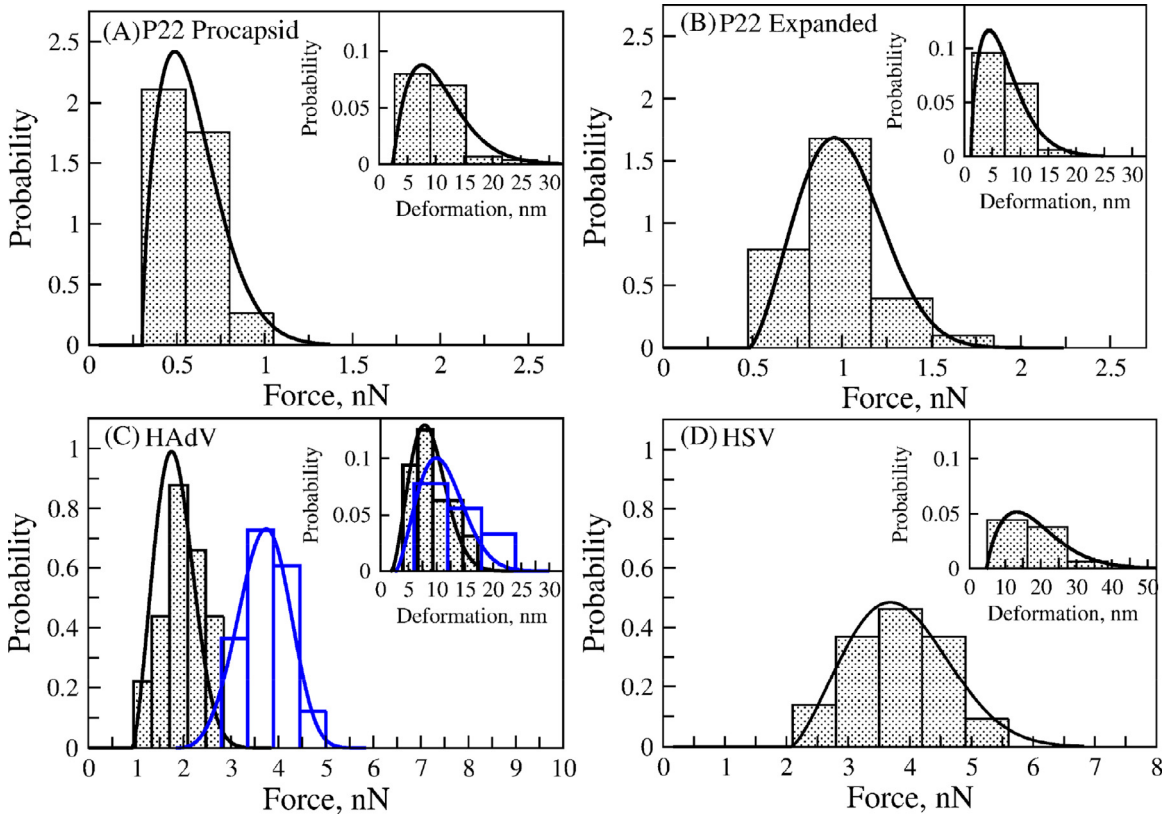

Fig. 3. Statistics of critical forces and critical deformations. Compared are the experimental histograms (bars) and theoretical curves (lines) of the probability density functions of critical forces $p(F)$ and critical deformations $p(X)$ (shown in *the insets*), obtained using Eqs. (13) and (14), respectively, for bacteriophage P22 Procapsid shell (**A**) and Expanded shell (**B**), Human Adenovirus capsid (**C**), and Herpes Simplex virus capsid (**D**). For the Human Adenovirus shell, the histograms of critical forces and critical deformations and theoretical curves $p(F)$ and $p(X)$ corresponding to the lower and higher critical forces and critical deformations are represented by the solid black and blue curves, respectively (**C**). The bin size selection was performed as described in Ref. [69]. Theoretical curves of $p(F)$ and $p(X)$ were obtained by setting $m \approx 1$ in Eqs. (13) and (14). (For interpretation of the references to color in this figure legend, the reader is referred to the web version of this article.)

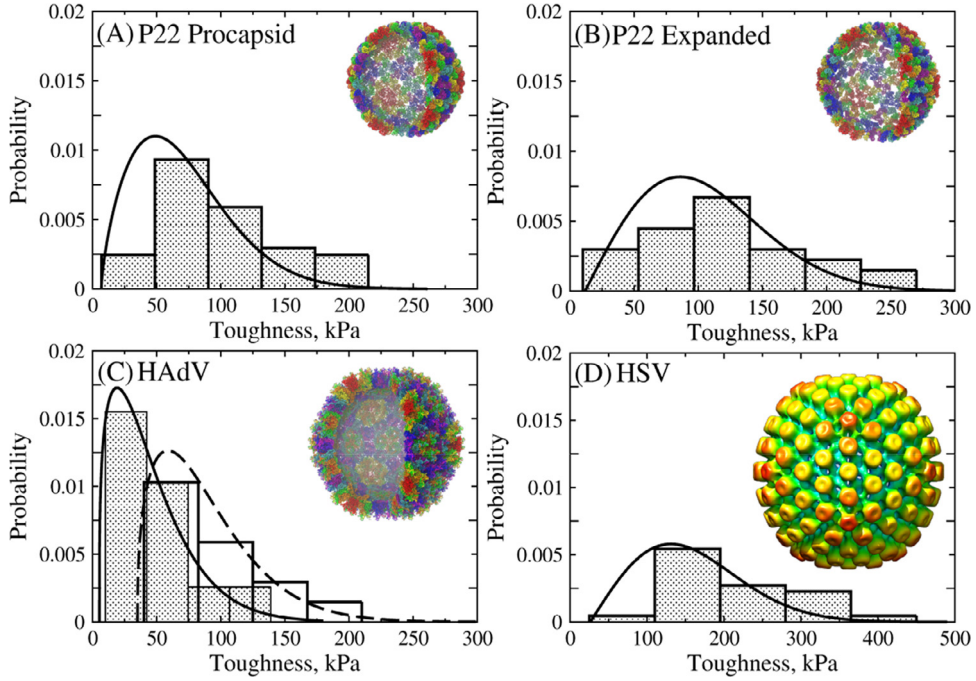

Fig. 4. Material toughness of biological particles. Compared are the experimental histograms (bars) and theoretical curves (labeled as in Fig. 3) of the probability density functions for particles' toughness $p(T)$ for bacteriophage P22 Procapsid shell (**A**) and Expanded shell (**B**), Human Adenovirus capsid (**C**), and Herpes Simplex virus capsid (**D**). The bin size selection was performed as described previously [69]. Theoretical curves of $p(T)$ were obtained by setting $m \approx 1$ in Eq. (17).

implying that higher peak forces do not necessarily imply larger critical deformation. For example, F_{cr} increases from 0.46 nN for Procapsid to 0.9 nN for the Expanded form of bacteriophage P22, whereas X_{cr} decreases from 9.8 to 6.2 nm (Table 1). Eq. (8) predicts that F_{cr} increases with increasing $\widetilde{F}_b$ and K_b (first two terms in Eq. (8)). In agreement with this notion, the numerical values of F_{cr} directly correlate with the values of $\widetilde{F}_b$ and K_b, meaning that larger values of K_b and $\widetilde{F}_b$ imply higher values of F_{cr} (Table 1). Eq. (9) predicts that X_{cr} is proportional to the ratio $\widetilde{F}_b/K_b$ (first term in Eq. (9)). This is true especially for capsids with smaller K_b (P22 shells); for larger K_b the contribution from the second term in Eq. (9) is large, and the relationship between X_{cr} and $\widetilde{F}_b/K_b$ is less straightforward (Table 1).

We used the FNS theory to estimate the Young's moduli associated with Hertzian indentation E_H and bending deformation E_b. The analytical expression for E_H reads [50]:

$$E_H = 0.75k_H\left(1-\sigma_H^2\right)\left(R_{par}^{-1}+R_{tip}^{-1}\right)^{-1/2} \tag{10}$$

where σ_H is the Poisson's ratio for the particle. The analytical expression for E_b is given by [33]

$$E_b = 16R_{par}^2K_b/\left(3\pi^2h^3\right) \tag{11}$$

The values of E_H and $E_b$are accumulated in Table 1. Based on Eq. (10), E_H is directly proportional to k_H but inversely proportional to the square root of R_{par}. Indeed, E_H increases from 0.03 GPa for P22 Procapsid to 0.27 GPa for HAdV, but then decreases to 0.17 GPa for the large 125-nm HSV capsid (Table 1). According to Eq. (11), E_b is directly proportional to the product of K_b and the square of R_{par}, but inversely proportional to the cube of h and so the dependence of E_b on K_b, R_{par} and h is less trivial. E_b increases from 0.25 GPa for the P22 Procapsid form to 1.86 GPa for the P22 Expanded form due mainly to the three-fold increase in K_b (Table 1); then, E_b decreases to 0.5–0.8 GPa for the HAdV capsid (Table 1) due to the three-fold increase in h from ~3.5 nm to ~9 nm (see Fig. 1); and then increases to 10 GPa for the HSV capsid due to a decrease of h to 4 nm.

Thermodynamics of deformation of biological particles: When the quasi-equilibrium conditions are met, the area under the average *FX*-spectrum is equal to the reversible work of particle deformation, i.e. $w_{rev}(X)=\int_0^X F(X')dX'$, which is equal to the equilibrium free energy change $w_{rev}(X)=\Delta G_{eq}(X)$. The slow experimental force-loading conditions (probe velocities v_f = 0.06–0.15 μm/s) make it possible to extract the free energy change for particle deformation from the *FX*-spectra. By performing the integration over X in Eq. (7), we obtain the closed-form expressions for free energy changes:

$$\Delta G(X)=\begin{cases}\frac{2}{5}B_0X_H^{*\,5/2}, & 0\le X\le X_H^* \\ B_0\left(X_H^*\right)^{3/2}\left(X_b^*-X_H^*\right)+\frac{1}{2}B_1\left(X_b^*-X_H^*\right)^2, & X_H^*<X<X_b^* \\ -\frac{2}{5}B_0\left(X-X_b^*\right)\frac{5}{2}+B_2\left(X-X_b^*\right)^2+B_3\left(X-X_b^*\right), & X_b^*\le X\le X_{cr}\end{cases}\begin{matrix}\\ (regime\ I)\\ (regime\ II)\\ (regime\ III)\end{matrix} \tag{12}$$

In Eqs. (12) above, the pre-factors B_0, B_1, B_2 and B_3 and the boundaries X_H^* and X_b^* separating the dynamic *regimes I* ($\le X_H^*$) and *II* ($X_H^*<X<X_b^*$), and *regimes II* and *III* ($X_b^*\le X\le X_{cr}$), are defined in Eqs. (7).

We used Eqs. (12) and parameters of the FNS model k_H, K_b and $\widetilde{F}_b$ from Table 1 to calculate the free energy changes for the Hertzian regime (ΔG_H), bending regime (ΔG_b), and plastic deformation (ΔG_p) in the collapse regime. These quantities increase with the capsid size in the sequence from bacteriophage P22 to HAdV, and to HSV (Table 2). The smallest values of ΔG_H = 0.03 MJ/mol, ΔG_b = 0.92 MJ/mol, and ΔG_p = 0.57 MJ/mol are for the capsid of bacteriophage P22 in the Procapsid form, and the largest values of ΔG_H = 1.2 MJ/mol, ΔG_b = 5.1 MJ/mol, and ΔG_p = 8.8 MJ/mol are for the capsid of HAdV (strong state). For all particles studied, the values of ΔG_H are an order of magnitude lower than the values of ΔG_b and ΔG_p, which shows that the Hertzian indentation is a mechanically weaker degree of freedom and also explains why Hertzian degrees of freedom become excited first (Table 2). The increase in ΔG_b with the particle size R_{par} implies that larger particles are more resilient mechanically. A similar increase in ΔG_p with R_{par} shows that larger particles are more plastic compared to smaller particles (Table 2). Interestingly, ΔG_b is larger than ΔG_p for smaller capsids (bacteriophage P22) but smaller for larger capsids (HAdV and HSV). This points to an increasingly more important role of plastic deformation (versus elastic deformation) in the mechanical properties of larger particles compared to smaller particles (Table 2).

Statistics of mechanical strength and deformability of biological particles: We analyzed the strength and deformability of capsids of bacteriophage P22, HAdV, and HSV. The average strength is captured by F_{cr} (Table 1). The strength of particles increases with R_{par} (Fig. 1) from the weakest capsid of bacteriophage P22 in the Procapsid state (F_{cr} = 0.46 nN and R_{par} = 52 nm) to the capsid of HSV (F_{cr} = 2.6 nN and R_{par}= 125 nm). Yet, the stronger particle is the capsid of HAdV (strong state) with F_{cr} = 3.5 nN, which is the second largest particle after HSV with R_{par} = 95 nm. The average deformability is reflected in X_{cr} (Table 1), which increases with R_{par} from 9.8 nm for the smallest capsid of bacteriophage P22 in the Procapsid state (R_{par} = 52 nm) to 14 nm for the largest capsid of HSV (R_{par} = 125 nm).

The *FX*-spectra demonstrate large variability in the mechanical response of capsids of bacteriophage P22, HAdV, and HSV to the applied compressive force (Fig. 2). This is reflected, e.g., in large fluctuations of F_{cr} and X_{cr} shown for all virus particles tested mechanically (see also Fig. S2). Hence, theoretical modeling of the average *FX*-curves may not be sufficient to understand the statistics of critical forces and critical deformations. Therefore, we used FNS theory to derive analytical expressions for the probability density functions (or distribution) of critical forces $p(F)$ and critical deformations $p(X)$ (see SI for detailed derivation):

$$p(F)=\begin{cases}0, & F\le F_b^* \\ \frac{m}{\widetilde{F}_b}\left(\frac{F-F_b^*}{\widetilde{F}_b}\right)^{m-1}\exp\left[-\left(\frac{F-F_b^*}{\widetilde{F}_b}\right)^m\right], & F>F_b^*\end{cases} \tag{13}$$

and

$$p(X)=\begin{cases}0, & X\le X_b^* \\ \frac{3mk_H}{8K_b\left(X-X_b^*\right)^{1/2}}\left(\frac{K_b}{\widetilde{F}_b}\left(\widetilde{x}_b(X)-X_b^*\right)\right)^{m-1}exp\left[-\left(\frac{K_b}{\widetilde{F}_b}\left(\widetilde{x}_b(X)-X_b^*\right)\right)^m\right], & X>X_b^*\end{cases} \tag{14}$$

where $F_b^*=k_HX_H^{*\,3/2}+K_bx_b^*$ is the force threshold, below which the particle's collapse does not occur, and $\widetilde{x}_b(X)=\frac{3k_H\widetilde{F}_b}{4K_b^2}(X-X_b^*)^{1/2}+\frac{\widetilde{F}_b}{K_b}-\frac{9k_H^2\widetilde{F}_b^2}{16K_b^4}$. The derivation of analytical expressions for $p(F)$ and

Table 2
Thermodynamic free energy functions for mechanical deformation of P22, HAdV, and HSV shells, calculated using the values of FNS model parameters (from Table 1): free energies for Hertzian deformation ΔG_H, bending deformation ΔG_b, and plastic deformation ΔG_p, obtained with Eqs. (12), and the free energy for particle fracture ΔG_f. The values of ΔG_f obtained using Eq. (15) and by performing the numerical integration of the average experimental *FX*-spectra are separated by the slash.

Particle	Thermodynamic state functions			
	ΔG_H, MJ/mol	ΔG_b, MJ/mol	ΔG_p, MJ/mol	ΔG_f, MJ/mol
P22 Procapsid	0.03	0.92	0.57	1.52/1.45
P22 Expanded	0.07	1.11	1.02	2.22/2.3
HAdV weak	0.40	2.00	3.30	5.70/5.90
HAdV strong	1.20	5.10	8.80	14.8/14.4
HSV	0.71	4.90	6.89	12.8/12.4

$p(X)$ does not require the use of the weak coupling approximation ($m \approx 1$), and so we retained the m -dependence in Eqs. (13) and (14) above.

The histograms of critical forces and critical deformations for all protein shells compare well with the theoretical curves of $p(F)$ and $p(X)$ reconstructed using Eqs. (13)-(14) above (see Fig. 3). Both distributions $p(F)$ and $p(X)$ are broad, skewed to the right, and have long right tails, especially for the P22 Procapsid and HAdV capsid. This implies strong stochasticity of the deformation dynamics, which leads to the large variability in the mechanical response of all protein capsids analyzed. For example, for the P22 capsid the most probable critical force (i.e. the maximum of $p(F)$) is $\hat{F} = 0.5$ nN for the Procapsid form and $\hat{F} = 0.95$ nN for the Expanded form, while the standard deviations (widths at half height) are ~0.5 nN and ~0.6 nN, respectively. Similar correlations are obtained for HAdV and HSV: $\hat{F} = 1.7$ nN and 3.7 nN for the weak and strong states of HAdV and $\hat{F} = 3.8$ nN for HSV, with the standard deviations of ~1.0 nN and ~1.4 nN for the weak and strong states of HAdV capsid, respectively, and ~2.1 nN for the HSV capsid (Fig. 3). Similar findings are observed for $p(X)$. The most probable particle deformations for fracture (i.e. the maximum of $p(X)$) for the P22 capsid are $\hat{X} = 7$ nm for the Procapsid state and $\hat{X} = 4$ nm for the Expanded state, while the standard deviations are ~11 nm and ~9 nm, respectively. For the HAdV capsid, $\hat{X} = 8$ nm for the weak state and $\hat{X} = 10$ nm for the strong state and $\hat{X} = 13$ nm for the HSV capsid, with the standard deviations ~8 nm for the weak state and ~9 nm for the strong state of HAdV capsid, and ~16 nm for the HSV (Fig. 3).

Toughness of biological particles: Material toughness is defined as the amount of free energy per unit volume required to deform and fracture the material [52]. We used the FNS theory to estimate the material toughness of the virus shells. Our recent computer simulation studies showed that soft biological particles fracture when the indentation force reaches the maximum, $F(X_{cr}) = F_{cr}$, at the critical deformation $X = X_{cr}$ [37–39]. Therefore, using Eqs. (12) we can sum together all three free energy contributions ΔG_H, ΔG_b, and ΔG_p to obtain the average total free energy change associated with fracture of a biological particle,

$$\Delta G_f(X_{cr}) = \int_0^{X_{cr}} F(X)dX = \Delta G_H(X_H^*) + \Delta G_b\left(X_b^* - X_H^*\right) + \Delta G_p\left(X_{cr} - X_b^*\right) \quad (15)$$

The average toughness T can then be obtained as the free energy density for particle fracture,

$$T(X_{cr}) = \frac{1}{V}\int_0^{X_{cr}} F(X)dX = \frac{1}{V}\Delta G_f(X_{cr}) \quad (16)$$

where $V = 4/3\pi R_{par}^3 - 4/3\pi (R_{par} - h)^3$ is the volume of the particle's protein shell.

The theoretical values of free energy for particle fracture $\Delta G_f(X_{cr})$, obtained using Eq. (15) and the values of X_{cr} from Table 1, and experimental values of $\Delta G_f(X_{cr})$ from numerical integration of the average experimental *FX*-spectra, compare very well (Table 2). ΔG_f increases with the system size, i.e. the larger the capsid the greater the value of ΔG_f. Therefore, it is not unexpected that the HSV capsid – having the largest protein shell, has the largest $\Delta G_f = 12.8$ MJ/mol (Table 2). Interestingly, ΔG_f for the shell of bacteriophage P22 in the Expanded state (2.22 MJ/mol) is larger than that in the Procapsid state (only 1.52 MJ/mol). Hence, given a small size difference and protein shell thickness (Fig. 1), these numbers imply a substantial shell remodeling of the bacteriophage P22 upon expansion (Table 2). Also, ΔG_f for HAdV in the strong state (14.8 MJ/mol) is three-times larger than that in the weak state (5.7 MJ/mol). This shows that the energies required to deform protein shells indented along different symmetry axes might in fact be very different. Next, we calculated the values of toughness $T(X_{cr})$ corresponding to the critical deformations for fracture X_{cr} (taken from Table 1). The results of the calculation of T based on theoretical *FX*-curves and experimental *FX*-spectra, accumulated in Table 3, show very good agreement. Overall, T decreases with increasing system size and thickness, but a more detailed analysis reveals a complex dependence on R_{par} and h (Fig. 1). T first increases with increasing R_{par} from 79 kPa for the P22 Procapsid to 116 kPa for the bacteriophage P22 Expanded Capsid, then decreases with increasing R_{par} to 47 kPa for the Human Adenovirus capsid in the weak state, and then increases again to 118 kPa for the HAdV capsid in the strong state, and to 484 kPa for the HSV capsid (see Table 3).

Table 3
Material toughness and limits of mechanical strength and deformability of P22, HAdV, and HSV shells: the average toughness T, toughness threshold T^*, and toughness range $\tilde{T}$, and the lower bounds of critical forces F_b^* and critical deformations X_b^*. The value of T are calculated with Eq. (16) using theoretical and experimental estimates of ΔG_f taken from Table 2 (separated by the slash). The values of T^* and $\tilde{T}$ are obtained from the fit of theoretical distribution $p(T)$ Eq. (17)) to the histograms of toughness (Fig. 4). Theoretical estimates of F_b^* and X_b^* obtained with Eqs. (18) and ((19) and experimental values of F_b^* and X_b^* are separated by the slash.

Particle	Material toughness			Mechanical stability	
	T, kPa	T^*, kPa	$\tilde{T}$, kPa	F_b^*, nN	X_b^*, nm
P22 Procapsid	79/75	5	78	0.21/0.24	4.5/5.8
P22 Expanded	116/118	6	111	0.75/0.61	5.2/3.3
HAdV weak	47/48	5	42	1.29/1.05	5.4/5.1
HAdV strong	118/114	35	58.2	3.0/3.2	8.2/7.7
HSV	484/468	26	148	2.6/2.7	10.7/9.3

We modeled the probability distributions of material toughness $p(T)$ using the same (Weibull type) analytical form for $p(T)$ as for $p(F)$, i.e.

$$p(T) = \begin{cases} 0, & T \le T^* \\ \frac{m}{\tilde{T}}\left(\frac{T-T^*}{\tilde{T}}\right)^{m-1}\exp\left[-\left(\frac{T-T^*}{\tilde{T}}\right)^m\right], & T > T^* \end{cases} \quad (17)$$

with the toughness scale parameter $\tilde{T}$ and toughness threshold T^*, which can be determined from the fit of Eq. (17) to the experi-

mental histograms (see below). As in Eqs. (13) and (14) for $p(F)$ and $p(X)$, in Eq. (17) we retained the m - dependence to provide the most general expression for $p(T)$. We used Eq. (17) to model the experimental histograms of toughness for all protein capsids obtained by numerically integrating the experimental *FX*-spectra obtained (Fig. 2; see also Fig. S2). The profiles of distribution $p(T)$ are very broad and have long tails for all virus capsids analyzed (Fig. 4). The information about the width of $p(T)$ is contained in the toughness scale parameter $\tilde{T}$, which quantitates the toughness variability. $\tilde{T}$ ranges from 42 kPa for the HAdV capsid in the weak state to 111 kPa for the capsid of bacteriophage P22 in the Expanded state (Table 3). For the HAdV capsid, $\tilde{T} = 58$ kPa for the strong state but $\tilde{T} = 42$ kPa for the weak state (Table 3). The toughness threshold T^* is the smallest value of toughness and, hence, the lowest value of free energy density at which the capsid might fracture (Eq. (16)). The capsids of bacteriophage P22 in the Procapsid state and HAdV in the weak state are characterized by the smallest $T^* = 5$ kPa, while the capsid of HAdV in the strong state has the largest $T^* = 35$ kPa (Table 3). Surprisingly, the capsid of bacteriophage P22 in the Expanded form is the second toughest shell of all with the average toughness of $T = 116$ kPa; yet, this particle's fracture might occur when the energy density reaches a threshold as low as $T^* = 6$ kPa. Similarly, the capsid of HAdV in the strong state is the toughest to fracture with the average toughness of $T = 118$ kPa, but the capsid might fracture when the energy density exceeds a 35-kPa threshold (Table 3).

4. Discussion

The mechanisms used by a virus for genome delivery strongly depend upon the type of host to be infected. Eukaryotic viruses, which infect animal and plant cells, are engulfed by the host cell in a process called endocytosis and usually disassemble inside, releasing the genome. However, bacteria present a complex outer envelope, sometimes comprising several layers of proteoglycan and lipid membranes. As a consequence, their viruses (bacteriophages) cannot use endocytosis to translocate the nucleic acid. Instead, the DNA is usually injected through a complex apparatus (the tail), comprising several structural proteins arranged in different topologies [53] according to the characteristics of their host envelopes. Although the usual mechanism of DNA translocation is enzymatically driven [1], results for some bacteriophages indicate the possibility of a two-step push-pull mechanism [54]. While the pull mechanism involves the host machinery, the push would be an energy cost-free process triggered by the release of elastic energy previously accumulated in the capsid during the genome packing process [55]. Regardless of the specific mechanism of genome infectivity [56,57], any capsid's mechanobiology is likely to play an important role in its genome infectivity process. Although the AFM-based technology has enabled researchers to explore the mechanobiology of biological particles, there is no unified theoretical framework to interpret and model the experimental force-deformation spectra.

In our prior studies [33,36–39], we employed the mechanical nanomanipulations of particles *in silico* to illuminate the physical picture behind their structural and shape alterations. This approach also identified the important mechanical degrees of freedom (mechanical excitations) most relevant for the uniaxial compressive force-induced deformation of thick soft biological particles; in particular, those that we studied, the protein capsids of the plant viruse Cowpea Chlorotic Mottle Virus (CCMV), the bacterial cell organelle encapsulin, and the eukaryotic cell microtubule structural filaments. To map these observations into a rigorous mathematical framework, we developed the Fluctuating Nonlinear Spring (FNS) model [33]. This model considers a number of distinct dynamic features: the Hertzian indentation due to the particle-indenter physical contact, the bending deformation of the capsid's side portion due to stress propagation from the particle-indenter physical contact area to the other portions of the particle's structure, and the eventual structural collapse due to the particle's fracture from the stress above the critical threshold. Because the stress is accumulated predominantly in the top and side portions of the particle and because the side portion of the CCMV shell accounts for >90% of the entire structure, the mechanical deformation of the CCMV capsid due to the particle-substrate interaction is essentially masked. For this reason, in the FNS model we did not explicitly consider the particle-substrate interactions [58]. The FNS-model based theory can be used to describe the mechanical deformations of thick soft biological particles in the entire range of their dynamic regimes, i.e. Hertzian indentation, elastic deformation, and structural collapse, and allows one to mechanistically interpret the experimental (or simulated) *FX*-curves.

In our previous study [33], the theoretical *FX*-curves were constructed using numerical calculations. Unfortunately, this reduces the interpretability of the results obtained. However, by using the weak dynamic coupling approximation ($m \approx 1$) in the present study, we were able to take a step further towards constructing a fully analytically tractable theory and derived the closed form expressions for the force-deformation lineshape (*FX*-curves), given by the master Eq. (7). Furthermore, we were able to obtain the closed form expressions not only for the average quantities but also for entire distributions of critical force, critical deformation, and fracture toughness. Moreover, we derived the analytical expressions for the free energy changes associated with the Hertzian indentation, bending deformation, and particle's fracture (see Eqs. (12)). The analytically tractable FNS theory can now be fully utilized to interpret and model the *FX*-spectra of biological particles, including the capsids of animal viruses, plant viruses and bacteriophages, and spherical cellular organelles, in all dynamic regimes of their uniaxial mechanical deformation. An experimentalist needs to model the average *FX*-profile. The model parameters obtained (as in Table 1) can then be substituted into the closed-form expressions to calculate the various mechanical and material characteristics of the biological particles.

An important element of the FNS theory is that it involves the survival probability Eqs. (4)-((6)), which links the dynamic structural alterations observed in biological particles to the stochastic nature of their deformations and builds elements of structural damage into the model to account for the particle's fracture. The survival probability also determines the fracture toughness of biological particles, which is widely used to describe the property of a material to absorb energy and to deform without fracturing. In the FNS theory (Eqs. (7)), there are three model parameters: the Hertzian stiffness k_H, the elastic constant K_b, and the force range $\widetilde{F}_b$ (Table 1). These can be used to calculate: i) the average critical force F_{cr} (Eq. (8)) and critical deformation X_{cr} (Eq. (9)); ii) the Young's moduli for Hertzian deformation E_H (Eq. (10)) and bending deformations E_b (Eq. (11)); iii) the distributions of critical forces $p(F)$ (Eq. (13)) and critical deformations $p(X)$ (Eq. (14)); and iv) the distribution of values of material toughness $p(T)$ (Eq. (17)). Moreover, the FNS theory can be used to calculate: v) the thermodynamic state functions, including the free energy changes associated with the Hertzian, elastic, and plastic deformations (Eqs. (12)), and the free energy for the particle's fracture ΔG_f (Eq. (15)). Using ΔG_f, vi) the average material toughness T (Eq. (16)) can be obtained.

We employed the FNS theory to analyze the experimental *FX*-spectra for the protein capsids s of Procapsid and Expanded bacteriophage P22, Human Adenovirus, and Herpes Simplex virus (Fig. 1). The Hertzian stiffness k_H directly correlates with the thickness h, whereas the elastic constant K_b correlates with the particle size R_{par}. The force range $\widetilde{F}_b$, which defines a physical range

of forces for the particle fracture, was also found to be directly proportional to the particle size (Table 1). We compared the average critical forces F_{cr} and average critical deformations X_{cr} for all protein capsids. Theoretical predictions for F_{cr} and X_{cr} agreed well with the experimental values of these quantities (Table 1) for all virus capsids analyzed. We found that F_{cr} and X_{cr} are uncorrelated, meaning that higher peak forces may or may not correspond to larger critical deformations. The FNS theory predicts that larger values of the elastic constant K_b and force range $\widetilde{F}_b$ imply higher peak forces F_{cr} (Eq. (8)) and that X_{cr} is proportional to the ratio $\widetilde{F}_b/K_b$ (Eq. (9)). These predictions were found to agree with the experimental data.

We applied the FNS theory to compare the mechanical strength of biological particles, which was found to vary in the nano-Newton range from the weakest capsid of bacteriophage P22 in the Procapsid state with the average critical force $F_{cr} = 0.46$ nN to the strongest capsid of HAdV in the strong state with $F_{cr} = 3.5$ nN (Table 1). Typically, ductile materials are characterized by large deformations of about 20% or more of their initial size, whereas brittle materials show little deformation that does not exceed 1% of their size [40]. The capsids of bacteriophage P22, HAdV, and HSV are not brittle, but rather weakly ductile with X_{cr} exceeding 10% (HAdV) to 19% (P22 Procapsid) of their size in the undeformed state. Because F_{cr} and X_{cr} are uncorrelated, this means that stronger shells might be less ductile, and hence, more brittle.

We used the FNS theory to compare the Young's moduli associated with Hertzian deformation E_H and with bending deformation E_b for all capsids. Bacteriophage P22 in the Expanded state is the second smallest capsid, but it was found to be the second most resilient particle in terms of bending deformation with $E_b = 1.86$ GPa, following the Herpes Simplex virus capsid with the largest bending modulus of ~10 GPa (Table 1). Surprisingly, we found that bacteriophage P22 in the Expanded state has the largest bending modulus (1.86 GPa) while being the thinnest particle of all those analyzed (Fig. 1). This can be explained, in part, by the presence of a large number of small protein protrusions on its outer surface, which might render the capsid structure to be more floppy and, hence, less compact (see Fig. 1D). The results obtained for E_H and E_b are entirely consistent with the theoretical predictions, namely that E_H is directly proportional to k_H but inversely proportional to the square root of R_{par} (Eq. (10)), whereas E_b is directly proportional to the product of K_b and the square of R_{par}, but inversely proportional to the cube of h (Eq. (11)). These findings also demonstrate the importance of distinguishing between the Hertzian mode (*regime I*) and bending mode (*regime II*) of deformation.

The FNS theory allows one to calculate the thermodynamic free energy functions for the Hertzian indentation (ΔG_H), elastic deformation (ΔG_b), and plastic deformation (ΔG_p). These quantities increase with the particle size R_{par}, thus, confirming that the free energy is an extensive quantity (Table 2). The Hertzian deformation is a mechanically weaker degree of freedom, which becomes excited first due to the indenter-particle coupling, prior to particle bending. Interestingly, the lowest values of ΔG_H, ΔG_b, and ΔG_p were obtained for the smallest particle (P22 Procapsid), but the highest values were found for the second largest HAdV capsid in the strong state, not the largest Herpes Simplex Virus capsid (Table 2). This points to the thermodynamic importance of favorable protein-protein interactions between the different capsomer units, which enhances the stability of protein capsid. The observed increase in ΔG_b and ΔG_p with R_{par} implies that larger particles are more mechanically resilient and, at the same time, more plastic compared to smaller particles (Table 2). The observed increase in the ratio of the free energy changes associated with plastic vs. elastic deformation, $\Delta G_p/\Delta G_b$, points to the importance of plastic deformation (compared to elastic deformation) in the nanomechanics of large biological particles.

We also analyzed the statistics of critical forces and critical deformations. Theoretical profiles of the probability distributions of critical forces $p(F)$ and critical deformations $p(X)$ for all protein capsids were found to be broad with long (right) tails. The most probable values of critical forces (~0.46–3.5 nN) and critical deformations (~5–12 nm) are different from their average values (~0.5–4 nN and ~6.2–14 nm; see Fig. 3 and Table 1); and are comparable with the standard deviations of critical forces and critical deformations (Fig. 3). These findings imply strong stochasticity of the dynamics of fracture of these protein capsids. The FNS theory allows one to estimate the force threshold F_b^* and the deformation threshold X_b^* below which the particle fracture does not occur:

$$F_b^* = k_H X_H^{*\,3/2} + K_b x_b^* = \widetilde{F}_b - \left(\frac{9k_H^2}{16K_b^3}\right)\widetilde{F}_b^2 + \left(\frac{27k_H^4}{512K_b^6}\right)\widetilde{F}_b^3 \tag{18}$$

and

$$X_b^* = \frac{1}{K_b}\widetilde{F}_b - \left(\frac{27k_H^2}{64K_b^4}\right)\widetilde{F}_b^2 \tag{19}$$

Eqs. (18) and (19) above can be used to find the limits (lower bounds) of mechanical strength and deformability of biological particles. We used Eqs. (18) and (19) and parameters of the FNS model (Table 1) to predict the lower bounds for critical forces F_{cr} and critical deformations X_{cr} for all virus capsids. The obtained values of F_b^* and X_b^* compare well with the minimum values of these quantities extracted from the experimental *FX*-spectra (Table 3).

The FNS theory allows for direct calculation of the material toughness of biological particles. Our recent *in silico* studies of the CCMV capsid [36,39] and microtubule filaments [38] demonstrated that soft biological particles fracture and collapse when the indentation force reaches the critical threshold F_{cr} (force peak in the *FX*-spectrum). Therefore, the experimental *FX*-spectra and FNS theory can be used to estimate the material toughness of biological nanoparticles. We compared the material toughness T for all virus capsids and found that, because T is an intensive variable ($T = \Delta G_f/V$), it displays a non-trivial dependence on the particle size R_{par} and thickness h (Fig. 1). Overall, T decreases with increasing R_{par} and h. Interestingly, one of the toughest particles is the capsid of bacteriophage P22 in the Expanded form with toughness $T = 116$ kPa; it is also the smallest ($R_{par} = 57$ nm) and the thinnest ($h = 3.5$ nm) of all (Table 3). This particle's toughness is only 2 kPa lower than the 118-kPa toughness for the HAdV in the strong state. The largest capsid of Herpes Simplex virus with $R_{par} = 125$ nm is the most tough with $T = 484$ kPa (Table 3). We also analyzed the probability distributions of toughness values $p(T)$ for all protein shells. The long tails of $p(T)$ point to a large variability in the energy required to fracture a protein capsid and imply that fracture of biological particles is intrinsically stochastic.

The thin shell theory [50,59] is widely used to describe the mechanics of deformation of virus shells, but only in the *elastic deformation regime II*. This theory does not account for the non-linear *Hertzian deformation regime I*, which is more characteristic of thick protein shells. On the other hand, the all-atom and coarse-grained Molecular Dynamics (MD) simulations [39,60], and finite elements calculations [9,61] can be used to illuminate the nanoscopic mechanisms of fracture of biological particles. To the best of our knowledge, the FNS theory is the only theoretical framework, which incorporates in a single formulation all of the following: the small-amplitude Hertzian deformation, the large-amplitude elastic deformation, and the particle's fracture. In the continuum limit of thin shell theory, the elastic behavior of shells depends on the Föppl-von Kármán (FvK) number given by the ratio of stretching and bending energies [62,63], and the shell fracture occurs when the

FvK number exceeds some critical value. Given the current level of development of the single-particle experimental instrumentation, it is difficult to measure the stretching and bending energies of biological particles, and so the additional input from computational modeling is necessary. In this regard, the FNS theory provides analytical expressions not only for the force response F as a function of particle deformation X and the deformation ranges for all three *regimes I-III* (see master equations (7)) but also the formulas for the critical force and critical deformation (see Eqs. (8) and (9)). In the FNS formulation, the onset of particle's fracture can be accurately predicted using the information from the experimental FX-spectra. The extension of thin shell theory to thick shells should be used with caution, because, as MD simulations show, in thick shells the in-plane deformation and out-of-plane bending modes are strongly coupled in *regimes II* and *III* [33]. For thick shells, the following expression is used to relate the particle stiffness K_b and Young's modulus E_b, $K_b = \alpha(E_b h^2/R_{par})$, where the coefficient $\alpha \approx 1$. This formula can only be used in the limit of small deformations, and so it does not describe the fracture of a biological particle. We used this formula in *regime II* to compare the values of E_b obtained with the thin shell approximation and the FNS theory (see Eq. (11)). The obtained values of E_b are accumulated in Table 1, which shows that predictions of the shell approximation and the FNS theory agree when $\alpha = 0.2$–0.4 is used. This also correlates well with the 0.6–0.8-range of α used in Ref. [64].

Unfortunately, current state-of-the-art experimental techniques do not allow researchers to directly relate the mechanical and materials characteristics of viral capsids (Tables 1–3) to the infection process. However, overall, there is a clear connection between the capsid mechanics and the viral infectious pathway, and so the properties of the protein capsids we have quantitatively analyzed can be used to better understand the infection pathways. For example, bacteriophage P22 undergoes a maturation process from the Prohead to the Expanded state while packing its genomic double-stranded DNA (dsDNA). While the Prohead structures self-assemble inside the host bacterial cytoplasm, the Expanded capsids are responsible for genome transportation externally. During transmission from host to host, the Expanded capsid has to enable genomic survival under stringent ambient conditions, such as osmotic shocks, extreme pH values and temperature fluctuations, dehydration, etc. [65]. Therefore, the superior mechanical strength of bacteriophage P22 in the Expanded state is directly correlated with the necessity of genomic survival in such severe environments outside, but not inside the bacteria. Also, bacteriophage capsids are known to be subjected to an enormous internal pressure, due to the densely packed dsDNA, a physical feature they utilize to drive DNA into the host bacteria during the infection process. Hence, bacteriophage P22 in the Expanded capsid should be mechanically stronger and more resistant to the higher internal pressure than in the Prohead state. For the Human Adenovirus capsid, the influence of the maturation state and its proteins' structure on the mechanical properties is well known [19,21,22,32]. Besides the importance of maturation state in the infection capacity of Human Adenovirus, there are external and internal proteins that play specific functions during the infection process whose presence undoubtedly modulate the mechanical properties of the Human Adenovirus capsid.

5. Conclusion

We developed a theoretical foundation for modeling and interpretation of the force-deformation spectra of biological particles, such as protein capsids of plant and animal viruses, bacteriophages, and cellular organelles. Based on the Fluctuating Nonlinear Spring model [33], this theory offers a comprehensive platform to describe the dynamic mechanical properties of biological particles in the entire range of Hertzian, elastic, and plastic regimes of their compressive-force-induced uniaxial deformation. Here, we showed by combining single-particle experiments and theoretical modeling of their force-deformation spectra that the mechanical and material properties of biological particles can be extracted and analyzed. Protein capsids of plant and animal viruses and bacteriophages are organized by capsomers (i.e., pentamer and hexamer units in many cases) into discrete and spatially non-uniform multi-domain architectures with microscopic defects (Fig. 1). Under the influence of external mechanical factors, these defects grow into larger cracks [38,39], and the stress and strain fields surrounding these cracks are highly non-uniform [36].

We applied the FNS theory to several empty capsid model systems: bacteriophage P22, Human Adenovirus capsid, and Herpes Simplex virus capsid (Fig. 1). The results obtained show that closed shells of biological particles, such as viruses and bacteriophages, are soft biomaterials with the elastic modulus of ~1–2 GPa or less (Table 1) and have low toughness of ~40–120 kPa (Table 3). The particles' toughness is found to be inversely correlated with their size and thickness, and with their strength (Table 3) [34]. We did not detect any strong correlation between the extent to which a particle is ductile and its size (Fig. 1 and Table 1). The average critical forces F_{cr} and critical deformations X_{cr} were found to be uncorrelated. Hence, stronger particle might be less ductile and more brittle. The FNS theory provides a means to accurately estimate the force threshold F_b^* and deformation threshold X_b^*, which set the lower bounds (or limits) of their mechanical stability and deformability. Larger biological particles are found to be both more mechanically resilient and more plastic compared to smaller particles.

The scope of potential applications of the FNS theory is manifold. The FNS theory can be used to make experimentally testable predictions. For example, the information about Hertzian deformation allows one to estimate the particle's thickness. Using the maximum value of Hertzian deformation (X_H^*) as an estimate of particle's thickness, we obtained 4.0 nm and 4.16 nm for the thickness of P22 Procapsid and HSV capsids, respectively, which come close to the measured 4.5-nm and 4.0-nm values of their thickness (Fig. 1). The FNS theory can be used to estimate the free-energy change for a particle's maturation and the free-energy difference associated with that particle's deformation along different symmetry axes. For example, by using the state-function property of ΔG_f and values of $\Delta G_f = 2.22$ MJ/mol and 1.52 MJ/mol for the capsids of bacteriophage P22 in the Expanded and Procapsid states, respectively, we estimated the free energy for P22 capsid maturation, $\Delta G = (2.22 - 1.52)$ MJ/mol $= 0.7$ MJ/mol. Using values of $\Delta G_f = 14.8$ MJ/mol and 5.7 MJ/mol for Human Adenovirus capsids in the strong and weak states, respectively, we estimated that it takes $\Delta G = (14.8 - 5.7)$ MJ/mol $= 9.1$ MJ/mol more energy to fracture the Human Adenovirus capsid in the strong state compared to the weak state.

Beyond the scope of the present study, where the theory has been applied to spherical particles, in the future the FNS theory could be extended to describe biological particles of other regular geometries, such as cylinders (i.e., microtubules) or ellipsoids (i.e., certain cellular organelles).

Declaration of Competing Interest

The authors declare that they have no known competing financial interests or personal relationships that could have appeared to influence the work reported in this paper.

Acknowledgements

We thank Beate Sodeik (Medizinische Hochschule Hannover) for the collaboration on Herpes Simplex Virus and Joost Snijder

(Universiteit Utrecht) for the AFM experiments on these particles. This work was supported by the NSF (grant DMR-1505316) and NIH (grant R01HL148227) to VB, by the Spanish Ministry of Economy, Industry and Competitiveness projects (FIS2017- 89549-R; "Maria de Maeztu"), Program for Units of Excellence in R&D (MDM-2014–0377 and FIS2017–90701-REDT) and Human Frontiers Science Program (HFSPO RGP0012/2018) to PJP, and by Nederlandse organisatie voor Wetenschappelijk Onderzoek (NWO) Vidi grant to WHR. CSM and GNC were supported by grants Q19PID2019–104098GB-I00/AEI/10.13039/501100011033 and BFU2016–74868-P, co-funded by the Spanish State Research Agency and the European Regional Development Fund, as well as grants BFU2013–41249-P and BIO2015–68990-REDT (Spanish Adenovirus Network, AdenoNet) from the Spanish Ministry of Economy, Industry and Competitiveness; and the Agencia Estatal CSIC (2019AEP045). The CNB-CSIC was further supported by a Severo Ochoa Excellence grant (SEV 2017–0712).

Supplementary materials

Supplementary material associated with this article can be found, in the online version, at doi:10.1016/j.actbio.2020.12.043.

References

[1] S.J. Flint, V.R. Racaniello, G.F. Rall, A.M. Skalka, Principles of Virology, John Wiley & Sons., Washington D.C., 2004.
[2] A. Zlotnick, Are weak protein-protein interactions the general rule in capsid assembly? Virology 315 (2003) 269–274.
[3] W.R. Wikoff, L. Liljas, R.L. Duda, H. Tsuruta, R.W. Hendrix, J.E. Johnson, G. Stubbs, Topologically linked protein rings in the bacteriophage HK97 capsid, Chemtracts 14 (2001) 125–130.
[4] U.F. Greber, Virus and host mechanics support membrane penetration and cell entry, J. Virol. 90 (2016) 3802–3805.
[5] P.J. de Pablo, Atomic force microscopy of virus shells, Semin. Cell Dev. Biol. 73 (2018) 199–208.
[6] M. Krieg, G. Fläschner, D. Alsteens, B.M. Gaub, W.H. Roos, G.J. Wuite, H.E. Gaub, C. Gerber, Y.F. Dufrêne, D.J. Müller, Atomic force microscopy-based mechanobiology, Nat. Rev. Phys. 1 (2019) 41–57.
[7] O. Kononova, A. Zhmurov, K.A. Marx, V. Barsegov, Mechanics of viruses, in: Coarse-Grained Model. Biomol., CRC Press, 2017, pp. 367–416.
[8] O. Kononova, K.A. Marx, V. Barsegov, Nanoindentation in silico of Biological Particles, in: Appl. Nanoindentation Adv. Mater., Wiley Blackwell, 2017, pp. 393–428.
[9] I.L. Ivanovska, P.J. de Pablo, B. Ibarra, G. Sgalari, F.C. MacKintosh, J.L. Carrascosa, C.F. Schmidt, G.J.L. Wuite, Bacteriophage capsids: tough nanoshells with complex elastic properties, Proc. Natl. Acad. Sci. U. S. A. 101 (2004) 7600–7605.
[10] W.H. Roos, R. Bruinsma, G.J.L. Wuite, Physical virology, Nat. Phys. 6 (2010) 733–743.
[11] N. Kol, Y. Shi, M. Tsvitov, D. Barlam, R.Z. Shneck, M.S. Kay, I. Rousso, A stiffness switch in human immunodeficiency virus, Biophys. J. 92 (2007) 1777–1783.
[12] P.J. de Pablo, Atomic force microscopy of virus shells, Semin. Cell Dev. Biol. 73 (2018) 199–208.
[13] M. Marchetti, G. Wuite, W. Roos, Atomic force microscopy observation and characterization of single virions and virus-like particles by nano-indentation, Curr. Opin. Virol. 18 (2016) 82–88.
[14] A. Evilevitch, W.H. Roos, I.L. Ivanovska, M. Jeembaeva, B. Jönsson, G.J.L. Wuite, Effects of salts on internal DNA pressure and mechanical properties of phage capsids, J. Mol. Biol. 405 (2011) 18–23.
[15] M. Hernando-Pérez, R. Miranda, M. Aznar, J.L. Carrascosa, I.A.T. Schaap, D. Reguera, P.J. de Pablo, Direct measurement of phage Φ29 stiffness provides evidence of internal pressure, Small 8 (2012) 2366–2370.
[16] W.H. Roos, I. Gertsman, E.R. May, C.L. Brooks, J.E. Johnson, G.J.L. Wuite, Mechanics of bacteriophage maturation, Proc. Natl. Acad. Sci. U. S. A. 109 (2012) 2342–2347.
[17] M. Baclayon, G.K. Shoemaker, C. Uetrecht, S.E. Crawford, M.K. Estes, B.V.V. Prasad, A.J.R. Heck, G.J.L. Wuite, W.H. Roos, Prestress strengthens the shell of norwalk virus nanoparticles, Nano Lett. 11 (2011) 4865–4869.
[18] W.H. Roos, M.M. Gibbons, A. Arkhipov, C. Uetrecht, N.R. Watts, P.T. Wingfield, A.C. Steven, A.J.R. Heck, K. Schulten, W.S. Klug, G.J.L. Wuite, Squeezing protein shells: how continuum elastic models, molecular dynamics simulations, and experiments coalesce at the nanoscale, Biophys. J. 99 (2010) 1175–1181.
[19] J. Snijder, V.S. Reddy, E.R. May, W.H. Roos, G.R. Nemerow, G.J.L. Wuite, Integrin and Defensin Modulate the Mechanical Properties of Adenovirus, J. Virol. 87 (2013) 2756–2766.
[20] D. Denning, S. Bennett, T. Mullen, C. Moyer, D. Vorselen, G.J.L. Wuite, G. Nemerow, W.H. Roos, Maturation of adenovirus primes the protein nano-shell for successful endosomal escape, Nanoscale 11 (2019) 3799–3803.
[21] A. Ortega-Esteban, A.J. Pérez-Berná, R. Menéndez-Conejero, S.J. Flint, C. San Martín, P.J. de Pablo, Monitoring dynamics of human adenovirus disassembly induced by mechanical fatigue, Sci. Rep. 3 (2013) 1434.
[22] A. Ortega-Esteban, G.N. Condezo, A.J. Pérez-Berná, M. Chillón, S.J. Flint, D. Reguera, C. San Martín, P.J. de Pablo, Mechanics of viral chromatin reveals the pressurization of human adenovirus, ACS Nano. 9 (2015) 10826–10833.
[23] J. Snijder, K. Radtke, F. Anderson, L. Scholtes, E. Corradini, J. Baines, J.R. Heck, A.G.J.L. Wuite, B. Sodeik, W.H. Roos, Vertex-specific proteins pUL17 and pUL25 mechanically reinforce herpes simplex virus capsids, 91 (2017) e00123–17.
[24] W.H. Roos, K. Radtke, E. Kniesmeijer, H. Geertsema, B. Sodeik, G.J.L. Wuite, Scaffold expulsion and genome packaging trigger stabilization of herpes simplex virus capsids, Proc. Natl. Acad. Sci. U. S. A. 106 (2009) 9673–9678.
[25] C. Carrasco, A. Carreira, I.A.T. Schaap, P.A. Serena, J. Gómez-Herrero, M.G. Mateu, P.J. de Pablo, DNA-mediated anisotropic mechanical reinforcement of a virus, Proc. Natl. Acad. Sci. U. S. A. 103 (2006) 13706–13711.
[26] C. Carrasco, M. Castellanos, P.J. de Pablo, M.G. Mateu, Manipulation of the mechanical properties of a virus by protein engineering, PNAS 105 (2008) 4150–4155.
[27] J. Snijder, C. Uetrecht, R.J. Rose, R. Sanchez-Eugenia, G.A. Marti, J. Agirre, D.M.A. Guérin, G.J.L. Wuite, A.J.R. Heck, W.H. Roos, Probing the biophysical interplay between a viral genome and its capsid, Nat. Chem. 5 (2013) 502–509.
[28] M. Jiménez-Zaragoza, M.P. Yubero, E. Martín-Forero, J.R. Castón, D. Reguera, D. Luque, P.J. de Pablo, J.M. Rodríguez, Biophysical properties of single rotavirus particles account for the functions of protein shells in a multilayered virus, Elife 7 (2018) e37295.
[29] J.P. Michel, I.L. Ivanovska, M.M. Gibbons, W.S. Klug, C.M. Knobler, G.J.L. Wuite, C.F. Schmidt, Nanoindentation studies of full and empty viral capsids and the effects of capsid protein mutations on elasticity and strength, Proc. Natl. Acad. Sci. U. S. A. 103 (2006) 6184–6189.
[30] J. Snijder, I.L. Ivanovska, M. Baclayon, W.H. Roos, G.J.L. Wuite, Probing the impact of loading rate on the mechanical properties of viral nanoparticles, Micron 43 (2012) 1343–1350.
[31] R. Vaughan, B. Tragesser, P. Ni, X. Ma, B. Dragnea, C.C. Kao, The Tripartite Virions of the Brome Mosaic Virus Have Distinct Physical Properties That Affect the Timing of the Infection Process, J. Virol. 88 (2014) 6483–6491.
[32] N. Martín-González, M. Hernando-Pérez, G.N. Condezo, M. Pérez-Illana, A. Šiber, D. Reguera, P. Ostapchuk, P. Hearing, C. San Martín, P.J. de Pablo, Adenovirus major core protein condenses DNA in clusters and bundles, modulating genome release and capsid internal pressure, Nucl. Acids Res. 47 (2019) 9231–9242.
[33] O. Kononova, J. Snijder, Y. Kholodov, K.A. Marx, G.J.L. Wuite, W.H. Roos, V. Barsegov, Fluctuating Nonlinear Spring Model of Mechanical Deformation of Biological Particles, PLoS Comput. Biol. 12 (2016) e1004729.
[34] J.Y. Sun, X. Zhao, W.R.K. Illeperuma, O. Chaudhuri, K.H. Oh, D.J. Mooney, J.J. Vlassak, Z. Suo, Highly stretchable and tough hydrogels, Nature 489 (2012) 133–136.
[35] H.J. Kong, E. Wong, D.J. Mooney, Independent control of rigidity and toughness of polymeric hydrogels, Macromolecules 36 (2003) 4582–4588.
[36] O. Kononova, F. Maksudov, K.A. Marx, V. Barsegov, TensorCalculator: exploring the evolution of mechanical stress in the CCMV capsid, J. Phys. Condens. Matter. 30 (2018) 044006.
[37] J. Snijder, O. Kononova, I.M. Barbu, C. Uetrecht, W.F. Rurup, R.J. Burnley, M.S.T. Koay, J.J.L.M. Cornelissen, W.H. Roos, V. Barsegov, G.J.L. Wuite, A.J.R. Heck, Assembly and mechanical properties of the cargo-free and cargo-loaded bacterial nanocompartment encapsulin, Biomacromolecules 17 (2016) 2522–2529.
[38] O. Kononova, Y. Kholodov, K.E. Theisen, K.A. Marx, R.I. Dima, F.I. Ataullakhanov, E.L. Grishchuk, V. Barsegov, Tubulin bond energies and microtubule biomechanics determined from nanoindentation in silico, J. Am. Chem. Soc. 136 (2014) 17036–17045.
[39] O. Kononova, J. Snijder, M. Brasch, J. Cornelissen, R.I. Dima, K.A. Marx, G.J.L. Wuite, W.H. Roos, V. Barsegov, Structural transitions and energy landscape for cowpea chlorotic mottle virus capsid mechanics from nanomanipulation in vitro and in silico, Biophys. J. 105 (2013) 1893–1903.
[40] P.J. de Pablo, The application of atomic force microscopy for viruses and protein shells: imaging and spectroscopy, Complement. Strateg. Understand Virus Struct. Funct. 105 (2019) 161–187.
[41] W.H. Roos, How to Perform a Nanoindentation Experiment on a Virus, in: G.J.L. Peterman, J.G. Erwin, Wuite (Eds.), Single Mol. Anal. Methods Protoc., Humana Press, Totowa, 2011, pp. 251–264.
[42] A. Llauró, D. Luque, E. Edwards, B.L. Trus, J. Avera, D. Reguera, T. Douglas, P.J. de Pablo, J.R. Castón, Cargo-shell and cargo-cargo couplings govern the mechanics of artificially loaded virus-derived cages, Nanoscale 8 (2016) 9328–9336.
[43] A. Llauró, B. Schwarz, R. Koliyatt, P.J. de Pablo, T. Douglas, Tuning viral capsid nanoparticle stability with symmetrical morphogenesis, ACS Nano 10 (2016) 8465–8473.
[44] A. Ortega-Esteban, I. Horcas, M. Hernando-Pérez, P. Ares, A.J. Pérez-Berná, C. San Martín, J.L. Carrascosa, P.J. De Pablo, J. Gómez-Herrero, Minimizing tip-sample forces in jumping mode atomic force microscopy in liquid, Ultramicroscopy 114 (2012) 56–61.
[45] J.E. Sader, J.W.M. Chon, P. Mulvaney, Calibration of rectangular atomic force microscope cantilevers, Rev. Sci. Instrum. 70 (1999) 3967–3969.
[46] I. Horcas, R. Fernández, J.M. Gómez-Rodríguez, J. Colchero, J. Gómez-Herrero, A.M. Baro, WSXM: a software for scanning probe microscopy and a tool for nanotechnology, Rev. Sci. Instrum. 78 (2007) 013705.

[47] G.N. Condezo, R. Marabini, S. Ayora, J.M. Carazo, R. Alba, M. Chillón, C. San Martín, Structures of adenovirus incomplete particles clarify capsid architecture and show maturation changes of packaging protein L1 52/55k, J. Virol. 89 (2015) 9653–9664.
[48] K. Radtke, F. Anderson, B. Sodeik, A precipitation-based assay to analyze interactions of viral particles with cytosolic host factors, in: C. Diefenbach, J. Russell, Fraefel (Eds.), Herpes Simplex Virus Methods Protoc., Springer, New York, 2014, pp. 191–208.
[49] K. Radtke, D. Kieneke, A. Wolfstein, K. Michael, W. Steffen, T. Scholz, A. Karger, B. Sodeik, Plus- and minus-end directed microtubule motors bind simultaneously to herpes simplex virus capsids using different inner tegument structures, PLoS Pathog. 6 (2010) e1000991.
[50] E.M. Landau, L.D. Lifshitz, Theory of Elasticity, Pergamon Press, 1986.
[51] E.J. Gumbel, Statistics of Extremes, Dover Publications, New York, 2004.
[52] J. Pelleg, Mechanical Properties of Materials, Springer Science & Business Media, 2012.
[53] M.F. Moody, Geometry of phage head construction, J. Mol. Biol. 293 (1999) 401–433.
[54] V. González-Huici, M. Salas, J.M. Hermoso, The push–pull mechanism of bacteriophage Φ29 DNA injection, Mol. Microbiol. 52 (2004) 529–540.
[55] D.E. Smith, S.J. Tans, S.B. Smith, S. Grimes, D.L. Anderson, C. Bustamante, The bacteriophage Φ29 portal motor can package DNA against a large internal force., Nature 413 (2001) 748–752.
[56] R. Zandi, D. Reguera, Mechanical properties of viral capsids, Phys. Rev. E. 72 (2005) 021917.
[57] M. Castellanos, R. Pérez, C. Carrasco, M. Hernando-Pérez, J. Gómez-Herrero, P.J. de Pablo, M.G. Mateu, Mechanical elasticity as a physical signature of conformational dynamics in a virus particle, Proc. Natl. Acad. Sci. U. S. A. 109 (2012) 12028–12033.
[58] X. Argatov, Jin I., Depth-sensing indentation of spherical particles on corrugated substrates — An asymptotic model, Int. J. Eng. Sci. 154 (2020) 103349.
[59] M. Aznar, S. Roca-Bonet, D. Reguera, Viral nanomechanics with a virtual atomic force microscope, J. Phys. Condens. Matter. 30 (2018) 264001.
[60] M. Zink, H. Grubmüller, Mechanical properties of the icosahedral shell of southern bean mosaic virus: a molecular dynamics study, Biophys. J. 96 (2009) 1350–1363.
[61] A. Ahadi, J. Colomo, A. Evilevitch, Three-dimensional simulation of nanoindentation response of viral capsids. Shape and size effects, J. Phys. Chem. B. 113 (2009) 3370–3378.
[62] J. Lidmar, L. Mirny, D.R. Nelson, Virus shapes and buckling transitions in spherical shells, Phys. Rev. E. 68 (2003) 051910.
[63] T.T. Nguyen, R.F. Bruinsma, W.M. Gelbart, Elasticity theory and shape transitions of viral shells, Phys. Rev. E. 72 (2005) 051923.
[64] M.M. Gibbons, W.S. Klug, Nonlinear finite-element analysis of nanoindentation of viral capsids, Phys. Rev. E. 75 (2007) 031901.
[65] M.G. Mateu (Ed.), Structure and Physics of Viruses, Springer, Netherlands, 2013.
[66] K.N. Parent, R. Khayat, L.H. Tu, M.M. Suhanovsky, J.R. Cortines, C.M. Teschke, J.E. Johnson, T.S. Baker, P22 Coat protein structures reveal a novel mechanism for capsid maturation: stability without auxiliary proteins or chemical crosslinks, Structure 18 (2010) 390–401.
[67] H. Liu, L. Jin, S.B.S. Koh, I. Atanasov, S. Schein, L. Wu, Z.H. Zhou, Atomic structure of human adenovirus by cryo-EM reveals interactions among protein networks, J. Sci. 329 (2010) 1038–1044.
[68] I. Ibiricu, J.T. Huiskonen, K. Döhner, F. Bradke, B. Sodeik, K. Grünewald, Cryo electron tomography of herpes simplex virus during axonal transport and secondary envelopment in primary neurons, PLoS Pathog 7 (2011) e1002406.
[69] E. Bura, A. Zhmurov, V. Barsegov, Nonparametric density estimation and optimal bandwidth selection for protein unfolding and unbinding data, J. Chem. Phys. 130 (2009) 015102.